TOPICAL REVIEW • OPEN ACCESS

3D optical measurement techniques

To cite this article: Thomas Engel 2023 *Meas. Sci. Technol.* **34** 032002

OPEN ACCESS
IOP Publishing
Measurement Science and Technology
Meas. Sci. Technol. **34** (2023) 032002 (26pp)
https://doi.org/10.1088/1361-6501/aca818

Topical Review

3D optical measurement techniques

Thomas Engel

Technology, Siemens AG, Munich, Germany

ennovare, Aalen, Germany

E-mail: engelthomas@siemens.com

Received 1 August 2018, revised 27 October 2022
Accepted for publication 2 December 2022
Published 28 December 2022

Abstract

The field of optical 3D metrology is gaining significant interest in the past years. Optical sensors can probe the geometry of workpieces and biological samples very fast, highly accurate and without any tactile physical contact to the object's surface. In this respect, optical sensors are a pre-requisite for many applications in the big trends like Industrial Internet of Things, Industry 4.0 or Medicine 4.0. The interest for optical 3D metrology is shifting from a metrology for quality assurance in industrial production to "digitize the real world" to facilitate a precise digital representation of an object or an environment for documentation or as input data for virtual applications like digital fab or augmented reality. The aspiration to digitize the world necessitates fast and efficient contact free sensing principles of appropriate accuracy for solid and even soft objects with a variety of colour, surface texture and lighting conditions. This review article tries to give a concise conceptual overview about the evolution of a broad variety of optical measurement principles that evolved and gained some importance in the field of 3D metrology for industrial 3D applications and their related technological enablers.

Keywords: 3D metrology, optical sensor, laser sensors, telecentric imaging, phase retrieval, digital calibration certificate, quality of sensing / data / information

(Some figures may appear in colour only in the online journal)

1. Introduction, general aspects for optical metrology

Many different optical measurement technologies were developed in the past years and decades. Figure 1 gives a coarse overview of the portfolio of technologies and base concepts being available in metrology products for industrial metrology applications today (see figure 1).

One major driver was to overcome the challenge to measure three dimensions precisely with a sensor or sensor array limited to maximally two lateral dimensions. The technologies range from single point measurements to systems with line sensor to measurement systems equipped with 2D image sensors for capturing geometric object information in three dimensions.

This review is focused on a selection of technologies to measure technical objects in various size ranges from micrometre to meters in lateral scale and accuracies from mm down to sub micrometre for some sensors. The selection of sensing concepts covered in this article can by far not be complete and exhaustive. It is oriented on typical metrological applications for industrial production and routine inspection applications and guided by the different technologies typically employed. This paper follows to some extent the evolution of significant

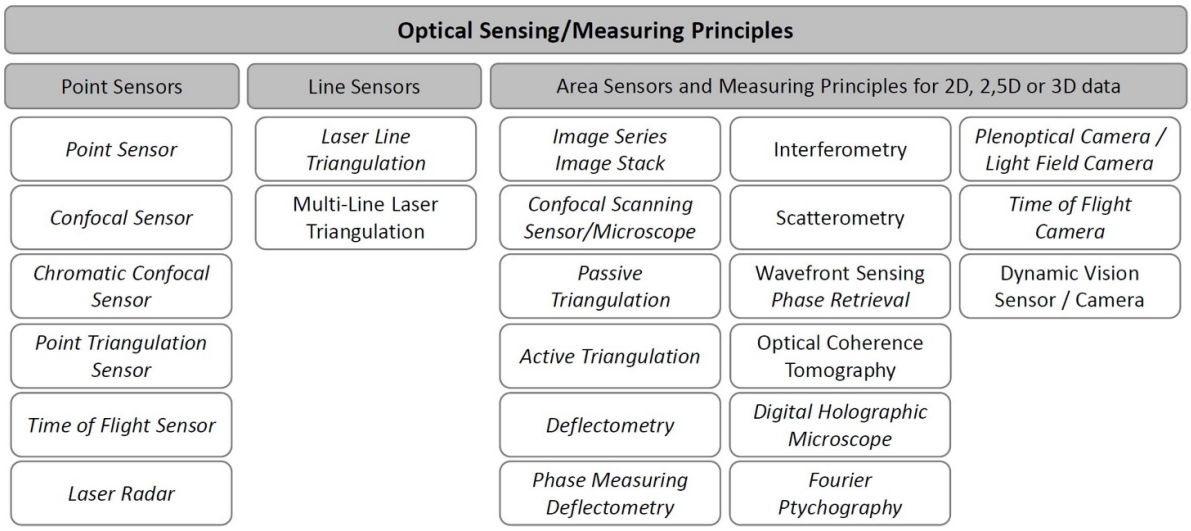

Figure 1. Conceptual and structural overview on the variety of optical one-dimensional to three-dimensional measurement technologies for industrial metrology application. Technologies printed in *italics* are covered in this article in more detail.

improvements and basic conceptual innovations of the different sensing principles over time. All technologies discussed in more detail in this review are printed in *italics* in figure 1. In the final section, some outlook on recently launched camera sensors may inspire passionate readers on how these sensors might improve the capabilities of the sensor systems described in the preceding sections even further. The later chapters of the middle section address some newer sensor types making intense use of a combination of physical sensors and a dedicated mathematical evaluation of the sensor's raw data to gain 3D metrological data. The last section also gives some outlook on the changes and opportunities we face, when the whole calibration chain gets digitized and digital calibration certificates (DCCs [1–3]) replace self-contained paper or pdf documents with calibration information. Finally, the concept of quality of sensing (QoS) and quality of data (QoD) gets introduced in order to convey further information related to the measurement or the data not directly impacting the measurement result and its uncertainty. Since this concept of these measurement related quality figures QoX is still evolving, it may change over time. The applicational aspects of the next section and the functional principles of the various sensor types may serve the reader as a basis to derive new and meaningful quality figures related to a specific measurement task.

Prior to a detailed view on the technologies selected, a short review of some applicational aspects might help the reader to compare and distinguish the respective technologies from a practical point of view. From a general point of view, the measurement task or the object to be measured might have significant impact on the technology selection in particular. Thus, a conscious consideration of applicational aspects might help to select the most appropriate measurement technique to a respective measurement task. This selection also might be supported by respective QoX indicators.

1.1. General aspects about optical measurements

The following section gives a short list of most relevant aspects when selecting, parameterizing and optimizing an appropriate measurement technology for a measurement task given:

1.1.1. Applicational aspects. Some of the measurement principles are capable of single frame measurement of an entire 3D scene. Other technologies need multiple frames or exposures or do a kind of serialized measurement by scanning the object with a line or a point. If the object to be measured is static and at rest, all technologies listed can be considered. For moving objects or when the object's shape is varying over time, like in some soft objects or even biological samples, the measurement time for a full data set has to be considered relative to the change rate on the object's shape. Typically, the respective measurement time has to be negligible relative to the time constant of changes of the object.

1.1.2. Accessibility. The geometry of the object to be measured also may imply some constraints to the measurement principle. Typically, the object's topography and geometrical structure defines an aspect ratio of widths vs. heights for the measurement. This ratio typically limits the applicable numerical aperture (NA) of the imaging system and thus controls the maximal achievable lateral and/or depth resolution. In classical imaging systems, the resolution is directly related to the NA or f-number (f#) of the optical system which are related by [4–8]:

$$NA = \frac{D}{2f} = \frac{1}{2f\#} \tag{1.1}$$

and in turn

$$f\# = \frac{f}{D} = \frac{1}{2NA}\ ,\ \textit{where} \tag{1.2}$$

f: Focal length of the optical system on object side D: Entrance pupil diameter of the respective optical system

1.1.3. Optical resolution criterions. When an object is imaged through an optical system, the lateral spatial resolution is given by the (equation (1.3)):

$$d = k1 \times lambda/NA \tag{1.3}$$

where lambda is the wavelength of light and NA the NA of the optics. The factor $k1$ determines the resolution limit depending on a criterion when two distinct points of an object are considered to be resolved in the image. In the image plane, for each point, there will be a diffraction pattern which can be described by the sinc-function [9, 10]. The closer the two points are to each other, the more the two diffraction patterns overlap. There are two prominent cases defining $k1$ relying on different models of the detectors used to observe the scene:

(a) In the case, that the peak of the one diffraction pattern coincides with the first minimum of the other pattern, then $k1$ becomes 0.61. It is the well-known Rayleigh's resolution criterion [11]:

$$d = 0.61 \times lambda/NA. \tag{1.4}$$

This criterion is very appropriate for observations by the human eye as a logarithmic scale detector. It is chosen very mindful but somehow arbitrary and other choices might be preferential for special cases. The remaining dip in the intensity from the peak to the center between the peaks is about 20%.

(b) For a linear detector $k1$ becomes 0.5, if the limit of resolution is assumed such that two incoherent diffraction patterns of two identical points are overlapped in a way that the profile of the signal summed up has a point of inflexion with a horizontal tangent at its maximum. This extremal case is known as Sparrow's criterion [12].

$$d = 0.5 \times lambda/NA. \tag{1.5}$$

It is related to typical electronic detectors like photodiodes, charge-coupled device (CCD) or complementary metal-oxide-semiconductor (CMOS) sensors which typically do have a highly linear signal response. Since this limit is the ultimate limit for diffraction-based imaging systems, it can be very much affected by noise, and it is hard to reach. This criterion is the limit typically applicable for electronic sensor based optical measurement systems.

The resolution criterion as selected as (a) or (b) sets a natural limit to the effective pixel size needed in the object space. A pixel is a single independent photosensitive element—like a photodiode—of a sensor array. Typical sensors consist of multiple pixels usually arranged in square matrix arrays.

The Nyquist–Shannon-theorem or the Whittaker–Kotelnikov–Shannon (WKS)-theorem [13] defines the physical resolution limit for classical imaging applications. Accordingly, a detector for measuring a spatially modulated signal/structure with a minimal feature size d has to have a pixel size smaller than half of the feature size d in the image space. Naturally, the imaging performance of the optics, especially the NA, has to be sufficient to image the structure of interest on the detector with sufficient resolution.

The depth of field concept (DoF) describes the depth resolution of an optical system. The DoF is a function of the respective wavelength lambda and the NA of the optics and often referred to as Rayleigh length [5, 8]:

$$DoF = \pm \frac{lambda}{NA^2}. \tag{1.6}$$

When discussing optical sensors, it is important to note, that lateral resolution and depth resolution scale with different powers of the NA in the denominator, as shown in equations (1.3) and (1.6). The resolution in both dimensions improves the higher the NA is but the depth resolution is much more nonlinear in its behavior.

In some special cases, other resolution criteria may apply for self-illuminated or fluorescent objects. There are some cases in microscopy where different resolution criteria apply, like for stimulated emission depleted microscopy [14, 15]. They are used for structural studies at cellular level based on sub resolution fluorescent light sources, bound to dedicated molecular structures. These technologies are not part of this review paper and therefore briefly mentioned for reference only on further options of microscopic measurements even below classical resolution limits.

1.1.4. Illumination vs. ambient light conditions. For optical measurements, the illumination conditions and the cooperativeness of the object to be measured and the respective wavelength and illumination type are crucial. Furthermore, ambient light can influence the results of a measurement significantly, since the background illumination can capture significant parts of the dynamic range of the detector. Thus, it reduces the signal to noise ratio (SNR) [16]. Even shadows can influence the measurement by pronouncing the object's topography and structure. To reduce or control the influence of theses external effects, some control measures typically get applied: enclosure of the measuring volume, apertures or spectral filters to minimize ambient light effects, minimize exposure times by use of high power or high flux illumination to optimize SNR or even pulsed illumination and synchronous sampling of measurement signal and background when the illumination is switched off.

1.1.5. Accuracy vs. time for measurement. The measurement time can affect the resolution of optical measurements directly by putting constraints on the exposure time of the sensor. The desired resolution and measurement accuracy usually depends on a minimum level of SNR. Proper signals can be achieved by employing light sources of sufficient light flux, optics of high transmission and high NA or low lens f# to collect as much light as possible but still fulfilling the demand on lateral sampling and sufficient DoF [17] for the respective application. Typically, it depends on the sensor principle, the sensor's mode of operation and the object itself, which of the methods mentioned can be employed. Key factors can be e.g. if

the object is stable or at rest or changing its shape or position over time. Such dynamic effects typically are acceptable when they are smaller than the nominal sensor resolution during one measurement or even one set of measurements with multiple exposures. Finally, a proper selection depends on the sensor working principle and relevant time constraints.

1.1.6. Properties of light. For the interaction of light with the object to be measured there are many contributing factors. On the one hand, there are the object properties like material, colour, surface finish or even surface coatings or contaminations and the properties of light as used for the measurement like wavelength, bandwidths, coherence in temporal and or spatial regime, polarization state and the sensitivity of the detector for the respective properties of light. Furthermore, the geometry of the whole imaging setup from the light source to the object and from the object to the detector defines the angular spectrum for illumination and imaging, respectively.

Therefore, it is an important prerequisite for an optimized selection of a sensing principle and related operational conditions of the sensor selected for a given measurement task and respective demand for accuracy, to take all these factors into consideration seriously. There is no one fits all solution for a general task of geometrical 3D measurements.

The main part of this review introduces and discusses different sensor technologies of great relevance in industry and some trends showing up. The order of presentation is somehow guided by the structural view on the sensor working principle as shown in figure 1 and the evolution of the measuring principles over time based on new technical capabilities coming up as sensor technologies evolved. The sensor types which are frequently used here are based on CCD [18] and CMOS [19] (Gen. 1–4). See also [20].

2. Point sensors

Early photoelectric sensors had only one or very few photosensitive elements. Consequently, point sensors were the first kind of optical sensors coming up for optical depth metrology. These sensors measure the distance from the sensor to a point on an object's surface along their optical axis. The surface position is assigned to the maximum intensity of the focus signal from a light spot irradiated on the object. Accordingly, these point sensors have to be moved along their optical axis in the direction of the object under test. The intensity signal representing the height is monitored with reference to the actual sensor position of the mover. Point sensors are performing well on optically cooperative surfaces. Figure 2 shows the functional principle of a basic version of this sensor.

Light of a light source is collected by a condenser lens, guided through a beam splitter to the objective lens focusing the light on an axial point along the optical axis. The light reflected and scattered at the object surface is re-collected by the objective lens when entering its aperture and is guided back to the beam splitter. Here, some portion of the light gets deflected into the sensing port, where a photodiode is positioned. Preferably, a focusing lens is located in front of the sensor

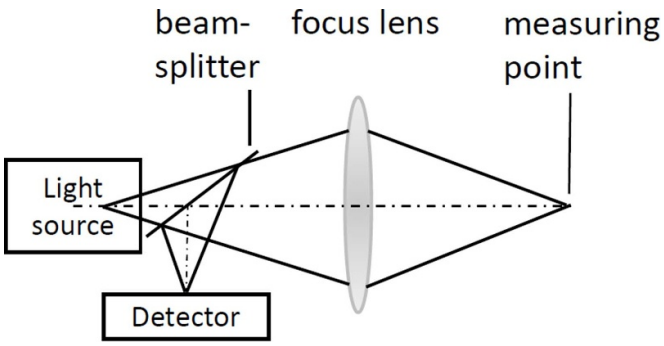

Figure 2. Schematic view of a basic point sensor.

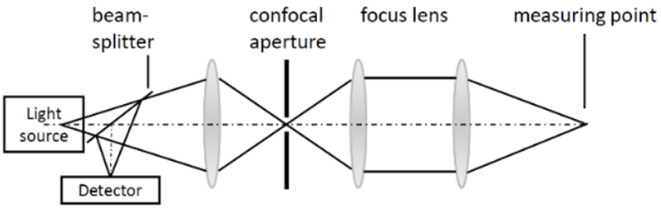

Figure 3. Schematic view of confocal point sensor.

plane to improve signal strength and signal quality resulting in shorter measurement times and increased sampling speed. To optimize signal quality further, the light source might be intensity controlled to adopt the sensor signal to the reflection and scattering properties of the object under test and thus improve the dynamic range of the sensor by the tuning range of the intensity of the light source. The surface position of the object is assigned to the maximum intensity reading of the photodiode. In a measurement cycle, the relative distance from the sensor to the object gets modified and the maximum intensity position gets detected. In essence, point sensors are single point detectors in lateral and axial direction with limited resolution capabilities especially for depth measurements. Accordingly, their success was quite limited over time and more versatile and thus more advanced sensing principles were developed.

2.1. Confocal sensors

To improve measurement accuracy in axial direction, a confocal aperture (pinhole) is added to the imaging setup of a point sensor in order to discriminate focused light from unfocussed portions and stray light. A discrete setup is shown in figure 3(A). Confocal sensors [21] can be quite sensitive to the respective imaging conditions, object specific effects and geometric obstruction. They are still single point detectors in lateral and axial direction so that they still need the measurement cycle as described above for axial and lateral scanning operations.

Optimization in the system setup splits the confocal aperture in two locations, one at the illumination side in light source and the other one on the imaging side coupled to the detector to simplify the setup. In case more advanced and more compact designs of fiber coupled sensor heads, the confocal

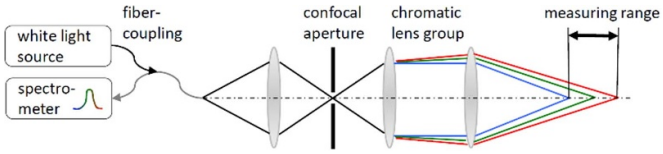

Figure 4. Schematic view of chromatic confocal point sensor.

aperture function is assigned to the fiber for both the illumination and the imaging side (figure 3).

2.2. Chromatic confocal sensors (CCS)

To relieve the strong constraint of a single measuring point in depth, chromatic confocal sensor, also known as confocal white light sensors, were developed. The core principle is sketched in figure 4.

The primary light source is a broadband light source like an arc lamp or LED with larger spectral bandwidth. The light of the light source is imaged on a pinhole, which serves as a spatially well-defined secondary light source. Later, the pinhole was replaced by the exit surface of an optical fiber. This secondary light source is positioned in a plane conjugated to the object plane. It is imaged by an optics specially designed with a predefined axial chromatic error. The axial chromatic dispersion creates separate focus regions for the different wavelengths of the light source along the optical axis. Preferably, the dispersion is quite linear throughout the spectral bandwidth used in the sensor. The amount of dispersion controls the respective shift in position for the axial image for given different wavelengths. Typically, the focus of blue light is closer to the lens than the red focus. In general, blue means shorter wavelength and red longer wavelength of the spectrum used, which is not necessarily in the visible spectrum. Depending on the measuring object or task, other wavelengths regions like infrared or deep blue to ultraviolet may be used, too. The advent of strong broadband LEDs helps to exploit these spectral bands with quite limited technical complexity compared to bulb lamps.

The axial distance from the blue to the red focus position spans the measurement range of the sensor. This line of chromatic foci as dispersed by the optics employed converts the single point confocal sensor principal for one wavelength into a sensor with a continuous measuring range along its optical axis for the respective spectrum of wavelengths. Its range is defined by design via the axial chromatic error of the imaging optics. The sensor's axial resolution can be defined by selecting the NA of the optics and the spectral resolution of the spectrometer appropriately. Compact spectrometers are built from line arrays of photosensitive elements plus a dispersive element, e.g. a grating to disperse the light traversing the pinhole or fiber. The lateral resolution of the confocal chromatic sensor is governed by the lateral spot size as a result of the lateral dimension of the pinhole or fiber core diameters, the effective magnification and the NA of the optics. The axial position measurement comprises of identifying and measuring one or multiple local maxima in the sensor's spectral profile as captured by the spectrometer. Due to the confocal setup of the sensor, light that gets reflected and/or scattered in focus for one wavelength at the object's surface is collected and re-focused on the pinhole or fiber core much more efficient than light from out of focus positions from other wavelengths.

Chromatic confocal sensors usually have comparably high NAs of 0.5 and above, thus the depth discrimination is fairly high since it scales with the second power of the NA according to equation (1.6). The chirp in wavelength along the sensors depth measurement range allows for a depth measurement by identifying the peak wavelengths for a specific sensor position. In principle, the sensor principle is capable to measure multiple peaks in parallel. The peaks correspond to multiple interfaces on the object's surface, like two sides of a foil, for layered material or surface coatings on a surface layer. Each peak corresponds to one interface of two neighboring layers with sufficient reflection, e.g. difference in refractive indices or other material properties in a stack of layers on the object. Since the spectral profile gets calibrated with respect to depth positions, different peak wavelengths correspond to different z-positions of the object structure. According to (1.1) and (1.2), the resolution is typically not constant along the measurement range, since the effective NA changes for the different wavelengths. The chromatic confocal sensor is well suited for fast scanning applications, since it can follow the surface topography of the object within its measurement range. Any deviation from a nominal set point can be used as control signal for a mover to re-position the sensor precisely along the optical axis. Chromatic confocal sensors play an important role for metrology due to high speed and high accuracy and precision even though the spectroscopic measurement adds some complexity and cost.

The advent of fiber-based spectrometers with fiber Bragg gratings (FBG) are an enormously powerful approach to build more compact, more robust, and cost-effective sensors since the whole spectrometer consist only of the fiber with the dispersive and focusing FBG and a line sensor affixed to the FBG portion of the fiber [22, 23]. The improved compactness is preferential also for robust applications in harsh and industrial environments. The integration of FBG spectrometer with a broadband LED is called interrogator which can be directly attached to the SMA fiber connector of many chromatic confocal sensors.

The depth measuring range of chromatic confocal sensors enables to measure a height profile of an object. This feature is used in the scanning confocal microscope [24] where two embodiments are shown in figure 4. The Nipkow-disc [25] is the lateral scanning element typically rotating at constant speed. It contains a lateral arrangement of spatially distributed pinholes of equal size which define separate equivalent but parallel imaging channels. The respective separation of the pinhole is big enough to prevent crosstalk of neighboring imaging channels on the one hand. On the other hand, the spatial distribution provides a uniform illumination of the object for the entire field of view (FoV). This necessitates, that the number of pinholes has also to increase with the disc radius to have the same amount of time a pinhole in the beam path to any portion to the sensor for a full revolution of the scanning disc. The

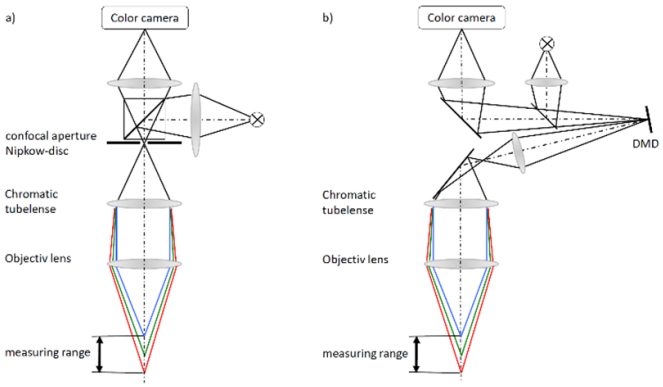

Figure 5. Schematic view of a scanning confocal microscope with (a) Nipkow-disc and (b) DMD as the scanning device.

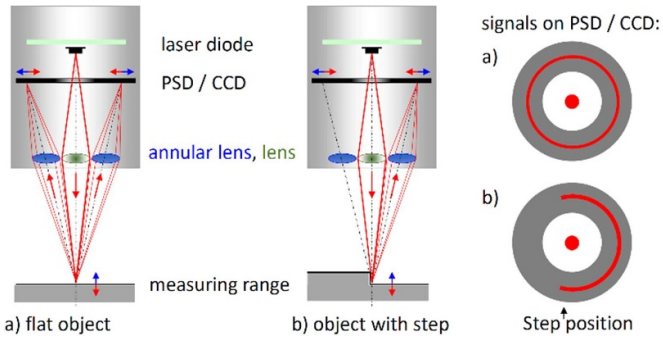

Figure 6. Schematic view of a triangulating point sensor for (a) a flat object and (b) a step in the object surface. The right column shows the respective light pattern on the detector [29].

camera is synchronized with the Nipkow-disc to always capture a full number of revolutions for uniform image illumination. Powerful light sources are employed for short exposure times to compensate for the significant intensity loss at the pinholes of the Nipkow-disc.

Alternatively, a digital mirror device (DMD) can be used as scanning device. It is used in reflective mode as shown in figure 5 on the right side. This makes the setup a bit more complex but allows for a digital control of the switch-on time for each imaging channel individual to allow for object specific illumination patterns.

By changing the magnification and/or NA of the objective lens or optics, the depth capturing range can be adjusted to some extend to the height span of the object's topography.

2.3. Triangulating point sensor

The triangulating point sensor is an alternative to the CCS sensor. In case of a step in the object's topography in the vicinity of the measurement point, partial obstructions in the aperture of the cone of light for the illuminating and/or measurement beam path (see figure 6) could have impact on the measurement accuracy and peak detection. To overcome this problem, a more advanced sensor scheme for a triangulating point sensor was developed [26]. The advent of position sensing detectors (PSD) [27, 28] had the potential to change the axial point sensor design into a more robust one. A PSD is a photodiode with a resistive layer on its backside. The photocurrent gets split in the resistive layer by the inverse ratio of the respective distance from the light spot to the neighboring pairs of electrodes. In consequence, the position where light is impinging on the photo detector can be directly calculated from the ratio of the photocurrents. Thus, a one-dimensional position measurement is feasible with an analog photodetector. For proper position measurements, the light does not need to be precisely focused on the PSD, but the light distribution needs to be within the spacing of the electrodes of the PSD. A schematic of this sensor is shown in figure 6.

A collimated or slightly focused beam of light illuminates the object. On the object's surface, the light gets reflected and/or scattered. This light is re-collected by a convex lens with annular shape. This annular lens images the light into a ring-shaped structure onto a PSD. The radius of this ring is measured with a PSD with annular electrodes. The radius is a direct measure for the distance of the object from the sensor. The closer the object is, the larger gets the radius of the ring. The further away the object is, the smaller the radius is. This measuring range allows to use this point sensor for scanning applications with a nominal set position in the middle of the measuring rang. Compared to tactile sensors for coordinate metrology, this feature corresponds to the transition from touch trigger probes to scanning probes and allows for much higher rates of points measured in a given time interval.

The resolution in the measuring axis is defined by the position measuring range and accuracy of the PSD, the focal length of the annular lens and the positioning of the lens with respect to the PSD. This sensor type can be easily calibrated and thus linearized with a flat object surface, e.g. of a gauge block, positioned at different distances from the sensor perpendicular to its optical axis. Preferably, the annular electrodes are segmented in multiple angular segments. There are PSDs available with multiple angular sectors like 4 quadrants. Accordingly, effects of partial obstruction can be identified simply by comparing signals from different sectors, which in turn improves the robustness of the signals and data quality inherently. In this sensor principle, partial obstruction in the beam path, e.g. by a step in the object's surface topography, can be determined directly from the sensor signals itself and thus the measured signals be qualified for trust level. This is a major improvement for all measuring applications. Due do the optical geometry of the sensor with on-axis illumination and off-axis detection by imaging with the annular lens, this sensor already belongs also to the class of triangulation sensors. Its strength is its scanning capability and robustness with respect to partial obstructions of the light in the measuring cone. In contrast to on-axis (confocal) point sensors with two major implicit restriction: (a) the illuminating beam spot is imaged directly and on-axis into a single spot on a photo detector and (b) this spot changes its center of gravity with degree and direction of partial obstruction, the triangulation sensor with segmented electrodes is able to infer a coarse annular position of the obstructing element and how strong the obstruction is. This information is also very valuable for scan path planning algorithms and for assessing the measurement quality.

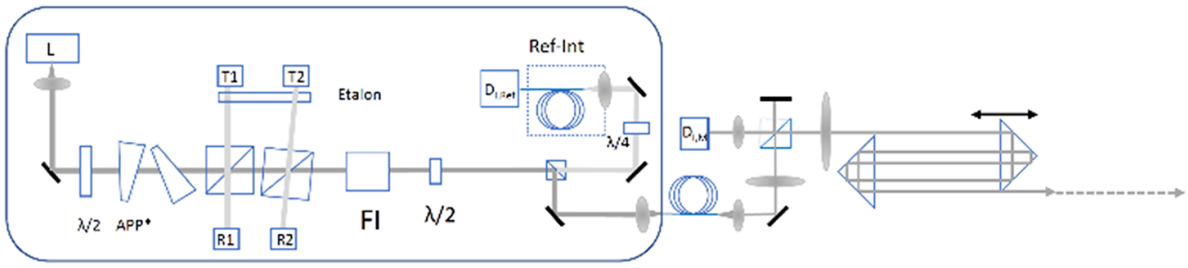

Figure 7. Schematic view of a laser radar with single laser L, half wave plate λ/2, anamorphic prisms APP, Photodiodes T1, T2, R1, R2 and $D_{I,\,ref}$ and $D_{I,M}$, faraday isolator, quarter wave plate λ/4 and a fiber based reference interferometer Ref-Int.

Photo sensors improved over time and increased its number of photosensitive elements, the pixels. Camera sensors with matrix arrays of photosensitive elements like CCD-sensors were employed to further improve the annular resolution of the triangulating point sensor by replacing the PSD for higher spatial sampling of the image of the ring-shaped structure. The higher number of sensor elements pushed the demand for faster signal transfer and image processing capabilities. The camera readout increased the sensor price significantly and did not improve its functionality so much.

2.4. Laser based point sensors

Lasers, especially compact and robust solid-state lasers, paved the way into a new class of point sensors. The temporal coherence of a laser is the enabler to measure a distance along a given axis with high precision. The second important feature of lasers is their capability for fast tuning while maintaining single mode operation. The emitted wavelength can be scanned over time with fairly high tuning rates in multi-MHz/s to GHz/s regimes fairly simple by manipulating the laser's control parameters like drive current, voltage or temperature appropriately to allow for fast scanning and still avoiding any mode hopping. Stable laser operation at pre-defined parameters is key to stable, robust and accurate measurements. Some applications are described in the next two sections in more detail.

2.4.1. Laser radar. Laser radars are used to measure distances with high accuracy in the single μm regime in a single axis direction. In a minimal setup as shown in figure 7 A, a single laser is used. It is scanned either in saw tooth or triangular mode. The scanning is monitored with two beams penetrating a solid etalon at slightly different angles to derive a sine and cosine signal in good approximation. To increase scanning quality over time, the etalon can be made of a material of low thermal expansion like quartz and/or temperature stabilized. The intrinsically nonlinear laser can be re-linearized by employing the sine- and cosine-like information to control the parameters of the laser driver by optimizing them for a constant change rate for the wavelength chirp. To protect the laser from light reflected back into the cavity, an optical diode is typically added.

The chirped laser beam (figure 7, [30]) is coupled into an interferometer either by free space coupling or by employing a fiber to decouple the two setups mechanically. The measuring head typically consists of a Michelson-type interferometer [5, 6] with a separate measuring and reference arm. The reference arm can be short, compact, and thus very stable. In the measuring arm, the beam is either collimated with a finite diameter or focused with a lens or zoom system to the respective measurement position in order to minimize the lateral dimension of the measuring spot at the position of the object to be measured. The light gets reflected or scattered back from the object and gets re-collimated by the aperture of the optics and re-united by the beam splitter with the reference beam. The resulting beam is directed onto a detector s. The temporal coherence of the laser must be big enough to cover the optical path difference in the two arms of the interferometer employed.

Due to the wavelength chirp of the laser, a distance between reference arm and measuring arm is converted into a beat frequency of the two beams, which can be directly measured by the detector. The beat frequency f is given by:

$$f = \textit{laser chirp rate} \times \textit{path difference} \times \frac{n}{c} \qquad (4)$$

where the path difference is the effective total path difference the laser light traverses on its way. It is typically two times the optical length difference of the two arms of the interferometer. n is the effective refractive index in the measurement arm and c the vacuum speed of light. Thus, the length measurement is converted into a frequency measurement, which can be performed with very high precision in a frequency range predefined by the chirp frequencies applied on the laser itself and the maximal measurement range.

Small changes in n, e.g. by local or temporal changes of temperature, pressure or humidity of air, will affect the measurement uncertainty and limit it in the low single digit micrometre range. Further measurement errors may occur, if there is a relative movement of the measurement head relative to the object in the direction of the measuring axis due to Doppler shift effects [31]. This can be determined either by repeated measurements in a fast sequence or by adding a second laser to the setup as shown in figure 8. If the first laser is chirped linearly in negative directions to lower frequencies, the second laser gets up-chirped to higher frequency with a different but known chirp rate. For a single object surface, this ends up in two beat frequencies measured on the detectors $D_{I,M}$ corresponding to the chirp rates of the to two lasers. Any Doppler shift will shift both beat frequencies in the same direction by

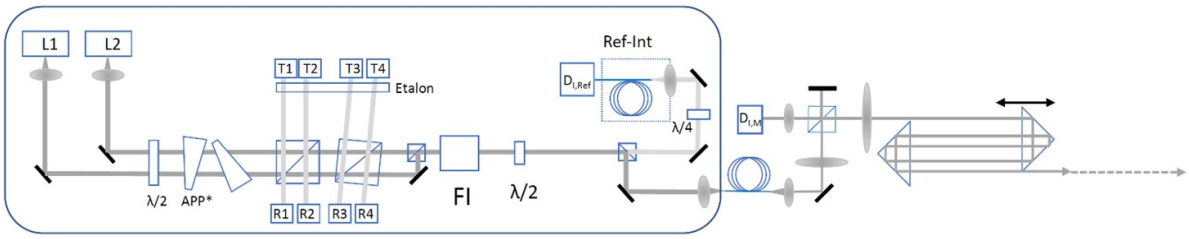

Figure 8. Schematic view of a laser radar with two lasers.

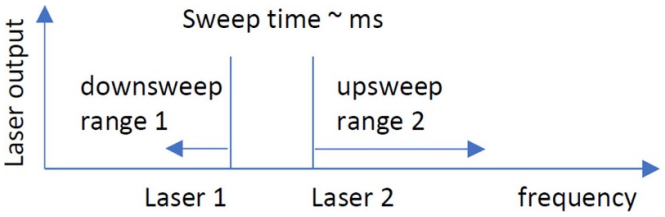

Figure 9. Concept for laser frequency scanning for the two lasers of the laser radar with two different sweep ranges.

the same factor. Thus, the Doppler shift can be deduced directly from the ratio of the two frequencies as measured by comparing it to the ratio of the nominal sweep scan rates. The length measurement value can be compensated for the motional effects accordingly. A schematic of the scanning frequency selection is shown in figure 9. Since the two lasers are incoherent with respect to each other, their wavelength can be chosen close to each other to minimize any dispersion effects in the measurement arm having considerable impact on the distance measured. To overlay the two laser beams, it is preferable to couple the laser unit with the measurement head through a single mode optical fiber.

The single mode fiber characteristic helps to reduce and even exclude any residual influences from any imperfect overlay of the two laser beams on the measurement.

2.4.2. Laser scanner. The laser scanner as sketched in figure 10 is based on the time of flight measuring principles. Typically, it measures the time delay between a short pulse sent out from an articulating scanning head and its reflection from the object surface when arriving back on the detector. The laser scanner utilizes laser diodes for their very fast switching capabilities to generate a pulse sequence of short light pulses of almost rectangular shape. Typical pulse widths are in the range of a few ten nanoseconds. The pulse is emitted from the laser, deflected in its direction of propagation by a two axis articulating scanning head, typically arranged as azimuthal and polar scanning axis. The scan unit is equipped with high resolution encoders to determine the laser's direction of propagation for the measuring axis with high precision in the range of arc seconds. The measurement is carried out in spherical coordinates with two angles and the distance as measured from the laser pulses. The measured system coordinates get converted into Cartesian coordinates in a post processing step.

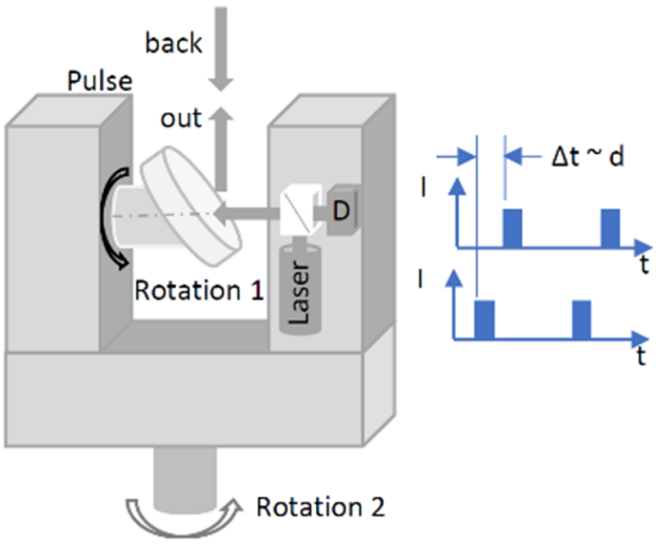

Figure 10. Schematic view of a laser scanner, D: detector.

The pulse delay measurement is very demanding, due to the high velocity of light with approximately 300 mm per nanosecond. Since the light is travelling the measuring distance back and forth, the measuring distance per nanosecond is 150 mm. This means, the bandwidth and sampling speed of the detection system has to be in the range of a few 10 GHz, when distances down to 5 mm and below have to be measured. For high precision measurements, the non-ideal pulse shape with limited slope steepness and the effects arising from reduced amplitudes of the returning signal due to scattering, reflection and absorption on the measurement pathway have to be considered when determining the final measurement result and its accuracy.

These effects typically get compensated for in the system signal processing chain while generating the measurement results for the distance. The pulse frequency, which results in the coordinate sampling rate of the sensor, can also be quite high, since the light travels so fast. For 30 m measuring range, the sampling time is approx. 180 ns, which means that scanners could use a sampling rate of up to 5 MHz for separate measurements.

From an applicational point of view, laser scanners are very useful, since they do not require any special preparation of the measurement object. They can be installed easily in a scene and a measurement can be started right away. The accuracy

is in the range of low single digit millimetres for the most advanced systems. Typical sources for measurement uncertainty like pressure or humidity of the air, disturbances of the measuring direction due to air streaks etc are typically still one order of magnitude lower than the mm resolution over the measurement range.

Thus, they do not need to be considered in more detail for most of the applications. Some advanced systems already compensate for air temperature or pressure influences. Therefore, laser scanners are very mature and versatile systems to digitize real world scenarios in 3D data point clouds.

2.4.3. Laser tracer. A laser tracer makes use of the laser radar concept and couples the measuring head to a gimbal mount. It swipes the laser beam in different directions by two angular coordinates to span a spherical coordinate system together with the radial distance measured. The gimbal typically has a vertical rotational axis for 360 degrees carrying a second rotational axis of $\pm \leqslant 90$ degrees for the inclination of the beam direction. This system steers the laser beam precisely into 3D space in order to measure the axial distance with respect to a reflector with high precision in the micrometre or even sub-micrometre range. For beam steering control and for tracing a retroreflector on a measurement object, there is a position sensitive sensing unit built into the setup. It detects any lateral offset of the beam coming back from the retroreflector. A spatial offset occurs in a retroreflector any time when the beam is not hitting the reflector on its optical axis. Thus, the pointing direction of the laser beam is actively controlled and set such that there is no or minimal lateral offset for the laser beam coming back from the retroreflector. This step is important since a laser tracer measures the optical lengths with interferometrical precision.

The laser tracker is designed to measure positions in 3D space. It can be easily applied to measure the motion characteristics and aberrations of a mover like a tooling or coordinate measuring machine (CMM) with linear and/or rotational axis. For the measurement, the mover under test is positioned at a sequence of different nominal positions and the laser tracer is capturing the real position information for each mover position in its spherical coordinates. Then, the laser tracer is repositioned at a second location and the set of nominal positions is measured again. This step can be repeated multiple times for different positions of the laser tracer. Height and/or orientations of the laser tracer are changed for each set of measurements to optimize the data quality level. The datasets measured at different positions are computationally merged into one concise data set and an error motion map for the mover is created. This error motion map can be used for a numerical motion compensation for the mover, often referred to as computer aided accuracy. Numerical correction of the mover works very well as long as the mover is reproducible in its positioning characteristics over time.

For measuring a mover e.g. of a CMM or a machine tool like a turning or milling machine, a retro-reflector is mounted on the mover to be measured in its 3D motion and according to the procedure described above, the machine axis move the reflector to a sequence of nominal positions and the laser tracer is keeping track of its motion trace and takes a sequence of measuring points along the trace.

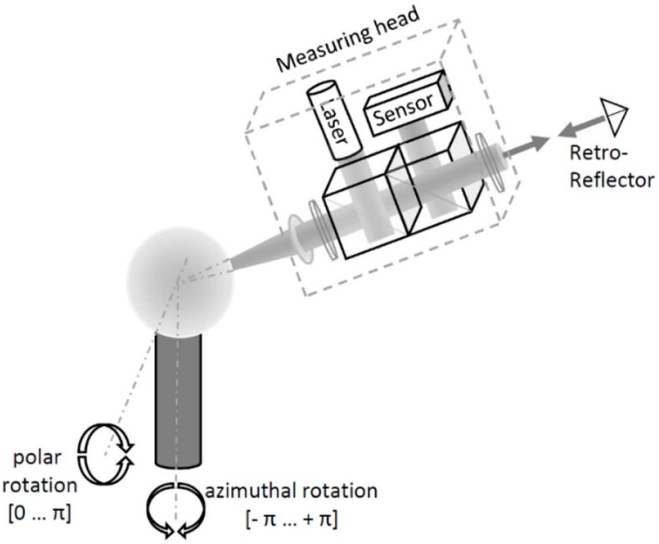

Figure 11. Schematic view of a laser tracer.

To optimize the measurement accuracy, the laser radar concept gets modified a bit. A precision sphere with exceedingly small form error replaces the reference mirror. The sphere center serves as the physical embodiment of the origin of the distance measurement. Thus, it is positioned mechanically and thermally stable in the center point of the gimbal spanning the spherical coordinate system as shown in figure 11. The measurement effectively starts at the sphere center and thus measures the entire distance optically. This leads to high resolution and accuracy in the sub micrometre range. To reach this accuracy level, the optical effects of the air penetrated on the measurement path have to be corrected for. This is typically done by temperature correction plus a second measurement wavelength. The two wavelengths are precisely known and referenced so that the differences in the measured values can be used to calculate for an effective refractive index of the air, which in turn can be used to correct the measured values effectively. By re-positioning the laser tracer at a second location, there is a second set of measured data. The relative position of the two measurement positions does not have to be known with high precision, since it can be calculated from the datasets as a translational fit parameter while merging the two datasets. This is possible if the number of data points equals or exceeds the remaining degrees of freedom. In case of motion characterization or when determining guideway aberrations of a mover with high precision and multiple measurement points on a line, this condition is fulfilled (figure 11).

The laser tracer concept is very appropriate for measuring volumes in the range of less than 1 m^3 to approx. 30 m^3, which relates to linear axis dimensions from a few 100 mm up to e.g. 3 m. For longer axis, the length dependent measurement uncertainty has to be taken into account and more effort has to be spent to have a reproducible measurement environment. This

is accomplished by compensating dispersion and/or air flow effects along the measurement path by employing multiple wavelengths for the measurement or fans to homogenize properties of the air in the measuring volume for the duration of the entire measurement cycle [32].

3. Line sensors

The demand to measure large areas and shapes in short time was the motivation to develop line sensors. Line sensors are capable of measuring a larger number of measurement points in parallel at the same time. Typically, the line sensing concept compromises a bit the accuracy achievable with point sensors and especially with confocal point sensors, but they are able to significantly increase the number of data points captured in a given time period by a factor of 1000 and above, depending on the optical camera sensor used. Another advantage of laser line sensors is the parallel measurement of multiple points at a time, which improves the results for moving objects or mobile measuring scenarios.

3.1. Laser line triangulation sensor

Laser line triangulation sensors as shown in figure 12 have a line projector projecting a trapezoidal fan of laser light into its measuring volume. The imaging optics of the sensor is arranged under a fixed inclination angle, the triangulation angle. It is set to image the entire depth of the measuring range of the sensor in a single frame on a 2D camera sensor. The width of the camera sensor corresponds to the direction of the laser line on the objects, the height of the camera sensor corresponds to the depth in the measurement range. The optics is gathering the light deflected and/or scattered from the object as it enters the entrance pupil. The optics is imaging a plane, which as tilted with respect to the optic's optical axis. To have a crisp image over the entire depth of the measuring range, a special imaging configuration known as Scheimpflug condition [33] has to be applied.

The Scheimpflug condition is formulated for imaging with a thin lens, that the object plane, the principal plane of the optics and the image plane have to intersect in one common line. Then, the image is sharp over the entire object area. Due to the inclination between object plane and lens, the distance from the object to the lens increases linearly with increasing depth in the sensor's measurement range. The increasing object distance from the lens leads to a reduced effective magnification in the imaging process according to the lens formula. This effect is called longitudinal magnification [5]. It is a nonlinear function and results in keystoning effects in the tilted object and/or image planes. Usually, the image sensor is a camera sensor of rectangular shape (figure 12).

When we trace the chip format back through the optics to the object plane, it is converted into a trapezoidal shape with the short side close to the sensor at the proximal end of the measuring range and the long side at the distal end of its measuring range, as sketched in figure 13 (left).

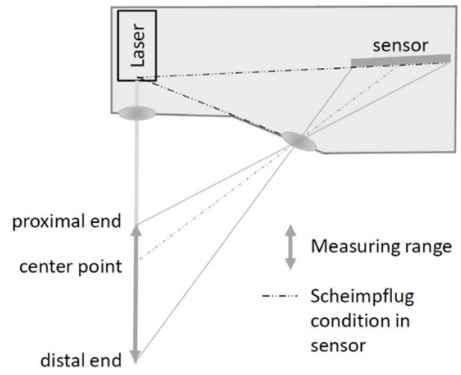

Figure 12. Schematic of a laser line triangulation sensor including the indication of the Scheimpflug condition.

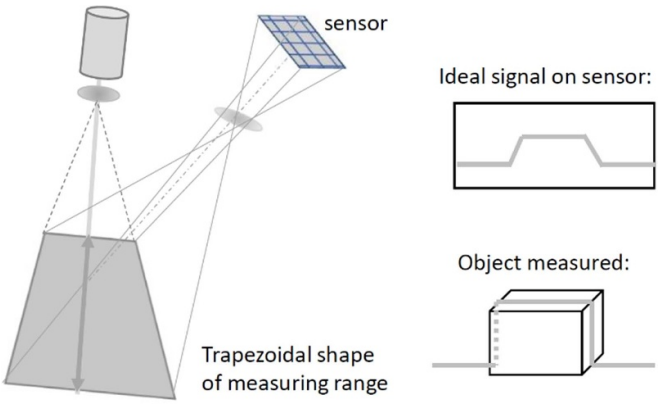

Figure 13. Left:3D schematic of a laser line triangulation sensor showing how the rectangular sensor is transformed into trapezoidal shape by the keystoning effect intrinsically related to the Scheimpflug imaging setup. Right: schematic of a rectangular bar as measured by the triangulation sensor and respective image on detector.

The camera chip determines the maximal frame rate of the sensor. To derive the desired depth information along the line, the peak position of the intensity profile is evaluated for each column of the camera sensor. The functional principal is sketched in figure 13 (right) for a rectangular shaped object. Due to the nonlinear depth scale in the image, the center of the chip is not the center of the measuring range. The proximal end of the measuring range is sampled with higher accuracy than the distal end and thus the mechanical center of the measurement range is shifted on the sensor closer to the side for the distal end.

This means, for most accurate measurements of an object, it is preferable to position the object's region of interest (RoI) close to the proximal end of the sensor's measuring range. On the other hand, the width of the laser lines reduces when going to the proximal end of the measuring range. If a given area has to be scanned in a given time, it could be necessary to compromise the achievable depth resolution and lateral resolution with the time available for the entire measurement. When scanning non-planar objects, the reflectivity or diffraction characteristics of the object may change with position. This may result in significant differences in the sensor signal

amplitude as a function of its position in the depth measuring range of the sensor. Accordingly, sensors with large dynamic range are preferred. This is supported by a trend in camera chip development for high dynamic range (HDR) cameras in recent years.

There has also been an alternative technology to generate the laser line on the object with an optical scanner like a rotating polygon. This results in a flying spot. The spot brightness can be controlled locally along the scan path at high speed. The benefit is a much higher dynamic range of the optical sensor by local and fast intensity control of the laser. This makes the sensor more versatile on surfaces with changing surface finish or mixed materials. The disadvantage is the introduction of moving parts from the scanner, additional weight and a limitation of the sensor capability to measure objects in relative motion to the sensor with high accuracy. The advent of cameras with high full well capacity and/or HDR reduced the importance of flying spot sensors in the past years. In these sensors, the imaging setup also is based on the Scheimpflug condition [33] with all implications mentioned above.

For the resolution of the sensor, the camera pixel size, the NA, and the triangulation angle from the camera's optical axis to the laser light fan are critical design parameters. The lateral and depth resolution scale linearly with the laser wavelength used, so that some blue light laser scanners appear on the market. The signal quality is a function of wavelength and the specific optical properties of the surface to be measured so that there is no general rule which wavelength is preferable. A solid housing with effective thermal positioning stability for all the components in the measurement chain is key for stable and reproducible measurements. High robustness of all the sensor geometry is essential for data post processing when rectifying the coordinates measured into the Cartesian coordinates in object space.

The desired signal mainly belongs to light scattered from the object's surface. Besides that, some portion of the laser light gets reflected. Dependent on the object's geometry, multiple reflections can occur which might deflect light back into the camera portion of the sensor. Typically, due to its reflective nature, this signal is much stronger in intensity and needs to be separated from the real signal to avoid erroneous results. Some peak detection algorithms showed up in some commercial sensors to detect the laser line and to differentiate multiple reflections in order to safely identify and evaluate precisely the correct peak location in the line of the scattered light of the real object surface [34, 35].

4. 2D and 3D sensors for areal and dimensional measurements

Areal measurement for a RoI at one instant of time is another key application for optical metrology. Typical systems scale from microscopic system with high magnification and aperture up to large area measurement systems with a FoV of many square meters. Since many methods used are functionally equivalent irrespective of the object size, they are treated in common in this section. When the FoV of the imaging system employed is not large enough to cover the entire RoI, stitching technologies might apply. To overlay and stitch images, some precise coordinate information is very helpful. Purely image-based stitching can be critical and hard to do in a metrological sense, since the imaging performance of optical systems typically degrades in contrast and/or distortion from the optical axis to the outer areas in the FoV in nonlinear, most often quadratic, manner. Therefore, it is preferred to rectify imaging distortions prior to stitching. This can be done by imaging a test pattern of qualified geometrical structure and is dealt with in special literature and standards like DIN EN ISO 10 360–7 [36]. Since imaging distortions are most often symmetrical, they double when combining regions from different FoVs from opposites sides of the optical axis.

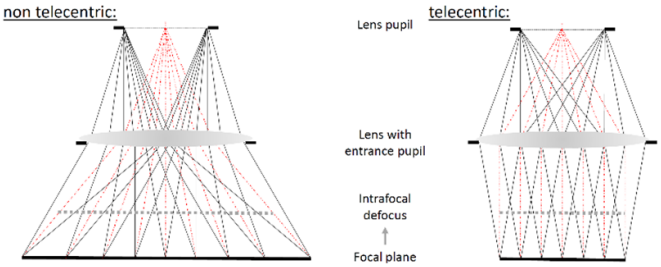

Figure 14. Comparison of non-telecentric and telecentric image cones on focal plane and in lens pupil.

4.1. Telecentric imaging

Telecentric optic is extremely useful for high precision dimensional and metrological imaging applications of objects. It minimizes the effect of defocus on the result of dimensional measurements. For telecentric optics, the cone of light captured and imaged from all different points of the FoV is the same. Their axis of symmetry is parallel to the optical axis of the optics as shown in figure 13. All points are imaged under the same condition. Due to the parallel cone axis of all light bundles in the object space, a slight defocus will not result in first order scaling errors over the entire FoV, i.e. with object height or topography. This improves the robustness of the imaging system to scaling errors significantly (figure 14).

Telecentric optics have one more constraint to the optical design to satisfy the tele centricity condition to have parallel cone axis over the entire FoV of the optics. Therefore, they need at least one more lens element, thus making the optics more expensive. In addition, as a direct consequence of the tele- centricity condition, the free diameter of a telecentric lens is always larger than the FoV plus twice the NA of the lens times its effective working distance. A coarse estimate is:

$$D_{\text{optics}} = D_{\text{FoV}} + 2NA\,d_{\text{working\_effective}}. \tag{5}$$

Due to the fixed term D_{FoV} for telecentric lenses, they are bigger in size than non-telecentric lenses where this portion can be reduced significantly. The bigger size causes more weight of the lens for the sake of spatially more homogenous imaging performance. Telecentricity can be used on the

object and/or the image side of the lens. For most applications, telecentric optics on the object side is sufficient. Image side telecentricity can reduce mechanical or thermal effects in the imaging system on the imaging plane position, e.g. from zoom tolerances or camera heating impact. Telecentric lenses can also be built as zoom lenses for variable magnification and/or working distance of the lens. The telecentric performance can be maintained for its zoom range—in very good approximation [37]. The optics can further be equipped with a projection unit for a scale reference to enable highly accurate measurements [38] even with different zoom settings. For precise measurements in different working distances, the illumination system has to be designed for nearly constant light budgets [39] over the range of working distances to minimize effects of the illumination on the measurement result.

Telecentric optics can increase the robustness of automated image processing and evaluation algorithms by constant imaging performance over the entire FoV. Technically, a constant image side NA over the zoom range of a lens may enhance this robustness even further, where the aperture is adapted to the optical resolution demand, e.g. as defined by a given camera pixel pitch.

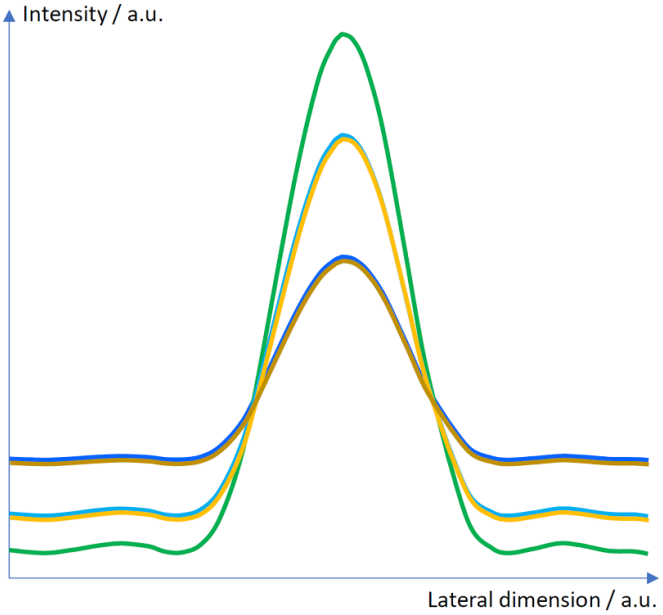

Figure 15. Schematic of typical through focus behavior of a pinhole or line image. Green—best focus plane, ±1 defocus in light and ±2 defocus in dark blue and yellow colour respectively. For larger defocus the intra- and extra-focal curves tend to deviate from each other with defocus.

4.2. From 2D to 3D imaging

Optical imagers with non-telecentric or telecentric optics take a flat two-dimensional view of a scene. The height or depth of an object's topography can be indirectly captured in the image as defocus, blur or scaling error and cannot be inferred from a single image without any additional technical means. In most cases, optical systems can 'only' image the object's topography as 2.5D image, when the object is not transparent to the wavelength used. Only for semi-transparent and transparent objects, the measured data can be 3D as volumetric or even tomographic data, showing internal structures of the object. If the information gained is 2.5D or 3D mostly depends on the object's properties and their specific interaction with the light used for the measurement. All methods discussed in the following sections are in principle capable of taking 3D data, which can be extracted by advanced data processing strategies. In the following, some commonly used strategies are presented and discussed with respect to functional principle and the respective aspects for their application.

4.3. Image stacks

To assess the 3D structure of an object, an easy and straightforward approach is to take a plurality of images in a focus series at different focus positions. An image stack preferably contains a plurality of images taken at the same FoV but with a constant defocus increment along the optical axis in z direction. The defocus typically scales with the DoF of the optics used as: $d_{\text{increment}} = s \times DoF$, where s is a scalar parameter in the range [0, 1] [40].

The image stack can be evaluated according to the needs of the application. To create an all-in-focus image—also called total focus image—for each location in the FoV a sequence of pixel exists from the different focus positions showing the intensity variation with defocus. Taking the extremal, i.e. maximal or minimal, intensity for the respective position and input it to a generic all in focus image frame creates a total focus image. Here all pixels are in focus irrespective of their height in the object itself. Naturally, the extremal intensity can be also derived from a numerical fit through the data points measured for each pixel to interpolate values to z positions not measured in the focus stack.

To generate a height representation of the object as topographic image, instead of the extremal intensities the related z positions of the respective image or from the interpolating fit over the defocus range are taken to generate the desired height profile image.

For semi-transparent objects with internal structure along the z-direction, the processing is technically the same, but more cumbersome. For pixels with 3D information, more than one extremal point can exist in the intensity profile over the defocus range. Thus, the profile has to be evaluated for multiple focus positions to generate a volumetric or tomographic image.

A third and very powerful method to determine dimensional metrics, like the width of an object structure, from a focus series is to overlay the line profiles through the feature of interest for all focus layers measured. This results in a plot as sketched in figure 15. Typically, the profile curves from different z positions intersect in a point or a quite precisely defined region. This point or region of intersection is almost not dependent on the focus position itself.

Thus, the related intensity value can serve as threshold value to measure the line width or other dimensional features of the structure very precisely and reproducible.

4.4. Phase retrieval, mathematical depth reconstruction

Usually, optical imaging systems do have some residual imaging errors stemming from imperfections of the lens, lens assembly or opto-mechanical setup like surface form, distance, centration or tilt. Therefore, for high precision measurements, it is desirable to determine and compensate for those errors. The error compensation stays valid, as long as the optical system has the same imaging performance over time. Typically, it means that the mechanical setup and interfacing of the system modules is highly reproducible.

The optical imaging performance can be measured with a through focus series of images on a special test target. The test method is known as wavefront sensing. It is the technical basis for the Hartmann [41] or Shack–Hartmann sensor [42, 43]. For the Hartmann sensor, a test target is a plane glass plate used in transmitted light imaging setting. On the glass plate, there are multiple sub resolution pinhole features whose dimensions are below the value as calculated from equation (1) with $k = 0{,}5$. Due to the small size of the pinhole, the light transmitted thorough a pinhole can be considered to be an ideal spherical wave. Consequently, it does not carry any deformation in the wave front after the pinhole. The light of this ideal point like light source transverses the entire imaging system and is captured on the camera sensor, where the sampling is preferably slightly better than governed by the resolution limit of the optics employed. Ideally, the through focus series is centered with respect to the best focus plane with a symmetrical number of image planes on the intra- and extra-focal sides. The images of the image stack measure the intensity I as the square of the complex amplitude A of the light field for every pixel position, i.e. $I = \mathrm{A}^* \times \mathrm{A}$. To determine the complex amplitude A of the light field from the multiple focal planes of known z-positions, a phase retrieval algorithm gets employed. These algorithms are typically based on the mathematical concepts for iterative phase retrieval by Levenberg–Marquardt [44, 45] or Gerchberg–Saxton [46] algorithm. In the phase retrieval, the intensity distribution measured in the image planes serve as boundary conditions in the iterations for the complex amplitude of the light field since the complex amplitude has to reproduce the intensity profiles as measured at the respective z positions. The phase retrieval results in a replication of the complex optical amplitude on the image side [47]. Since the object was ideal, a perfect imaging system would have created the images of multiple spherical waves over the FoV. By comparing the reconstructed optical field with that of the ideal spherical wave, the imaging errors can be determined and described in an appropriate base system to describe imaging errors, like the Zernike [48] or Seidel [5] imaging theory. Measurement accuracies down to a few 1/1.000 of the wavelength employed have been reached and confirmed with interferometrical measurements of the same lens in the same orientation. This means, that phase effects below 0.2 nm can be measured by this non-interferometric method [49]. This method is used for high quality optics to assess the image quality during fabrication and end testing.

When the imaging errors are properly measured and stable over time, they can be used to correct images of later measurements from the influences of the imaging system. Mathematically, it is a de-convolution operation between the image measured and the error function of the optics as determined. This is beneficial when aiming at the ultimate imaging performance for the lateral and/or depth resolution of the respective optics.

When the consecutive measurements on real objects are also through focus series, the formalism can be used to measure the phase of the object structure itself. This was done on lithography masks with feature sizes in the wavelength range, where interferometers cannot be applied to determine the height of a phase step of strong phase shift masks showing only phase effects [50]. Crucial for robust performance is a high SNR for the images taken since noise can affect the iterative reconstruction significantly.

When the complex optical amplitude A is known, it can be propagated and evaluated for a depth or height measurement of object structures even for z positions not directly covered by the focal planes in the image stack. This is an enormously powerful tool and method to measure height of an object without the need for an interferometer and thus without the impact of coherence effects like speckles on the image quality. In addition, small structures and feature sizes can be measured not accessible by interferometers [51].

5. 3D measurement technologies

5.1. Fourier ptychographic imaging

Fourier ptychography is a computational method to synthesize high resolution high NA images from low aperture images. A larger set of images is taken from an object under test with an imaging system of limited magnification and limited NA. A schematic setup of the minimal optical setup is shown in figure 16.

The input images are taken with Nyquist conform sampling to have correctly sampled images with full information content available from the optical system. The object is illuminated from a variety of different directions. Each direction provides spatially highly coherent illumination conditions, i.e. quasi collimated light beams illuminate the entire FoV of the optical system. Each image is illuminated with one or a low number of spatially well separated light sources where the angular separation of LEDs used is preferably maximally in the range of the imaging lens NA. Publications report on multi light source exposure of up to eight light sources in a single camera frame [52]. Multi-exposure can be a mean to reduce the effective number of frames below the number of high NA images needed and stitched in order to cover the same FoV by classical high-resolution imaging in the object space. Figure 17 shows the aperture filling and overlap for an array of 9×9 LEDs. Please note, the LEDs are not equally spaced in the spatial frequency domain in the aperture plane leading to a higher overlap for LEDs illuminating at larger aperture angle. This effect can be compensated for by an LED array with corrected positions for the LEDs with respect to NA.

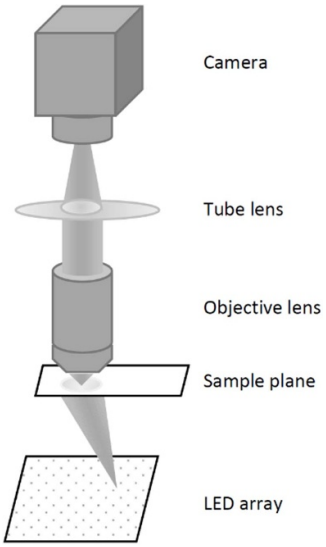

Figure 16. Schematic of a Fourier ptychography microscopes (FPM) with a flat array of LED light sources.

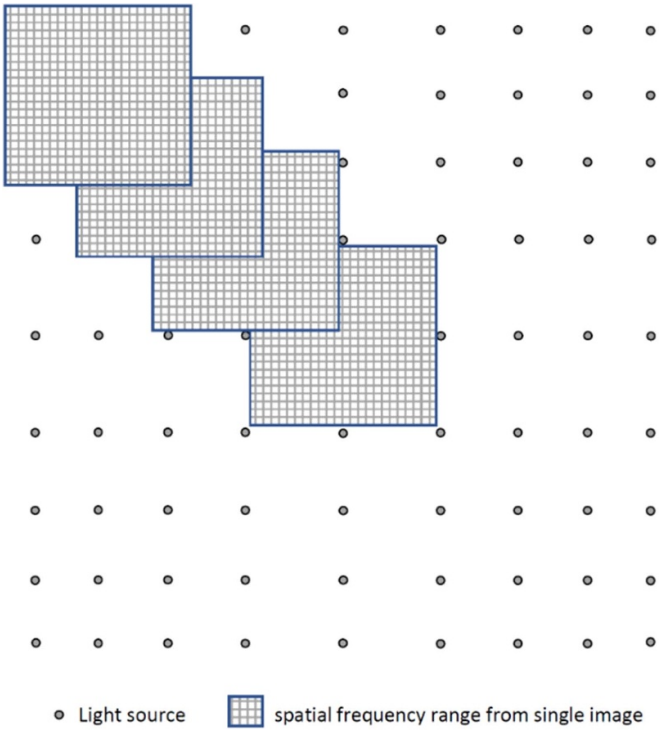

Figure 17. Schematic in the Fourier domain for stitching the image content for the LED illuminations of different angular positions.

The set of images plus the information on the spatial distribution of the light sources, its central wavelength or spectral characteristics and the respective intensities is input to an image reconstruction algorithm. Conceptually speaking, in the algorithm the image information is converted into an angular diffraction pattern for the respective wavelength, gets combined with the direction of the incident illuminating beam and is merged in self-consistent iterative optimization with all other diffraction patterns of the additional illumination directions. For stable results, an overlap of at least 50% of the angular frequency range of neighboring illumination settings has proven to be necessary. Typically, the reconstruction algorithm is a derivative form of Levenberg–Marquardt or Gerchberg–Saxton algorithm as its core. Since the angular frequency range is stitched together for the different illumination directions, the effective Fourier space is enlarging and thus the sampling accuracy is increased for the reconstructed image. This means, the reconstructed image of a Fourier ptychographic imaging system [53] has a higher spatial resolution than each of its input images it is based upon. The image synthesis results in a significant up sampling of the image sampling with an effectively reduced pixel size for the output image. For example, with an imaging system with NA 0.15 the images are taken. The reconstructed image is computed showing the same spatial resolution and details like images taken with an optical system having a NA of 0.9. Some authors also show images, where the effective NA has to be larger than 1 for the resolution attained on binary structures of a US Air Force (USAF) test target [54] in patterns of group 11 for the respective wavelength. This is quite remarkable for an imaging system without immersion and shows the potential of this computational imaging method, especially for the domain of microscopy where the method is called Fourier ptychography microscopy (FPM) [53]. The paper of Ou *et al* [55] with all references included gives a much broader and more detailed overview over this interesting topic.

Table 1. Comparison of typical performance parameters for a typical high aperture microscope and a Fourier Ptychography Microscope.

Parameter	Microscope	FPM
Main lens	40x/0.95	5x/0.15
Sampling according to Nyquist-Shannon theorem: $\sim 0.5 \times$ lambda/NA/2.5	109 nm	693 nm
Pixel size @camera/object	3.5 μm /88 nm	3.5 μm /700 nm
FoV for 10 mm chip size	0 0625 mm^2	4 mm^2
DoF (@520 nm)	$\pm$0.58 μm	$\pm$23 μm

When comparing a normal microscope with high NA and a FPM system, there are some major functional differences, which might be highly relevant for many applications. Due to the low magnification of the FPM, the FoV scales for the same camera chip by the squared ratio of the respective magnifications, i.e. $(M\_{Micro}/M\_{FPM})^2$.

Due to the low NA of the FPM microscope, the DoF is much larger by a factor $(NA\_{Micro}/NA\_{FPM})^2$.

When both systems take images at a given wavelength (e.g. 520 nm) by sampling at the Nyquist limit for a chip with given pixel size, we can directly compare the performance parameters of two typical sets of system configurations as shown in table 1.

The FoV is enlarged by a factor of 64 and the DoF by about 40 for the FPM. In order to properly stitch a larger microscope image, some overlap has to be taken into account. The

FPM system needs to take a few hundred images to properly reconstruct a high NA image, which is about a factor of 4–5 more than for the microscope. There is an option to reduce the number of input images by multi-exposures settings in one image frame to counteract this effect. On the other hand, these input images have sampled a DoF about 40 times larger than that for the microscope, making the FPM much more robust against focusing errors and to contrast tiny structures. The FPM preferably needs static objects when capturing the set of input images. Both systems have their strengths and weaknesses. Therefore, considered selection of a system depending on the requirements of the application is suggested. Due to the demand on the multiple light sources this method is applicable preferably in microscopic imaging scenarios, where the benefit under high NA conditions can make a difference.

The trend of large image sensors supports somehow the Fourier ptychography approach. For high NA optics with DoF below 1 μm or even 0.5 μm, i.e. in the range of a wavelength, a constant focus plane coinciding with the object over the entire FoV is getting harder to fulfill. Mechanical probe alignment, flatness of the sample or vibrations are typical limitations which is not so much an issue for low NA imaging in ptychography. The later can much easier make use of larger image sensors with high pixel number and small pixel size. Thus, reducing the demand for high magnification and in turn even expands the effective FoV further as discussed on our example. Typically, this optimization is limited by the dark current of very small camera pixels which in turn limits the SNR and thus the quality of the reconstructed image.

The quality of the synthesized image depends strongly on the SNR of the sub-images. When the illumination NA exceeds the imaging NA, it leads to dark field illumination settings. Thus, the light intensity captured by the imaging optics after being scattered or deflected by the object structure reduces strongly with increasing NA. This effect can be compensated by higher brightness of higher NA light sources and/or longer exposure times of the camera. Higher gain of the camera does not improve the SNR. The optimized and modified imaging parameters for illumination and camera have to be taken into account and compensated for in the reconstruction process.

Fourier ptychography can also be used to synthesize colored images. For each colour a separate reconstruction is performed. Then, the colour channels are merged into a colour image including the option for white balancing and setting the desired colour temperature. For optimized sampling, it is preferable to capture the input images with a respective bandpass filter on a B/W camera chip instead of interpolating between pixels of a colour camera sensor for each colour channel. This might introduce some sampling artifacts in the input images and to the iterative reconstruction process.

After reconstruction, a digital refocusing of the FPM image is possible to mimic the imaging performance of the microscope within the limited DoF. Alternatively, total focus images can be generated. For reconstructed images of high quality, the sub images of the FPM have to be tuned to optimal S/N ratio.

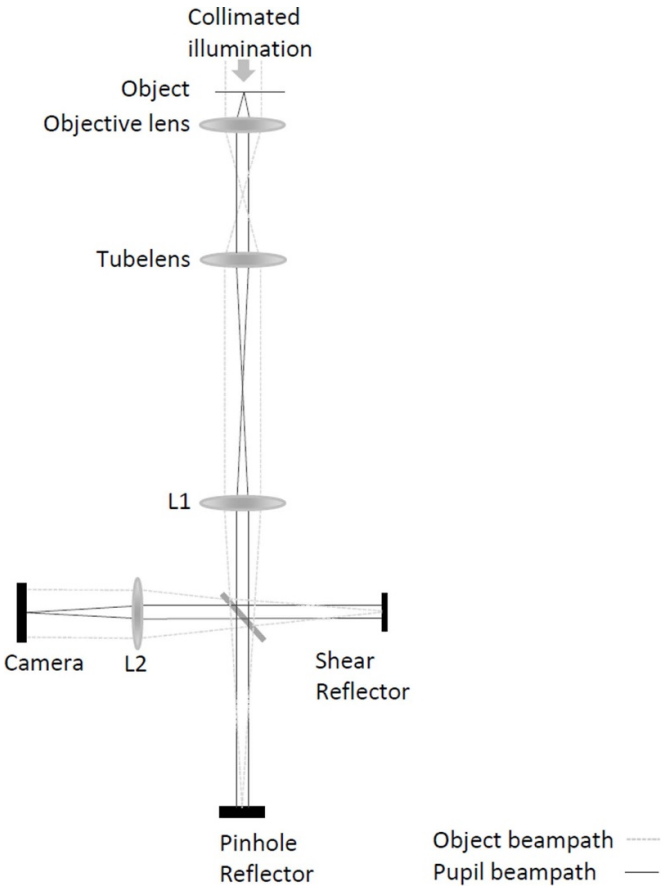

Figure 18. Schematic of a digital holographic microscope setup with indicated beam path for object (field) and pupil.

5.2. Holographic imaging

The combination of interferometry and microscopy in an imaging system bears a very powerful toolset to image and analyze small objects, especially small phase objects, with high resolution [56–58]. The interferometric principle to compare one portion of light interacting with the object with a second portion of light serving as reference wave of known shape enables to measure very small wavefront deviations of the two portions of light with respect to each other. The interaction with the object can be either in transmissive or reflective beam path arrangements. In the past, a very versatile micro-interferometer was a modular system from Carl Zeiss Jena, called Jenaval Interphako [59]. The input was the light field of an object as captured by a microscope lens. The Interphako module has many mechanical and optical manipulators to control shear and/or optical path length differences in a Mach–Zehnder type of interferometer. Dedicated optical experts were required to operate the purely manual system in order to create images of good contrast for the operator for a broad variety of objects.

Due to the advent of high-resolution camera chips, the idea of digital holography was born. Here, a camera captures the interference patterns from the optical field. A computer program is employed to evaluate these complex patterns. Finally, an image interpretable by a standard user is created. Figure 18

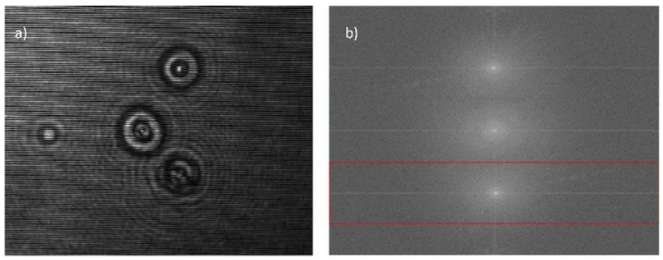

Figure 19. DHM image with horizontal shear fringe line (a) and (b) corresponding Fourier spectrum with central peak and the ± 1 side maxima in vertical axis related to the shear fringe pattern spatial frequency. Red box shows maximal cropping window for image evaluation and fringe pattern suppression.

shows a sketch of one embodiment of a digital holographic microscope [60]. Preferably, the light field is split up into two portions, the one is the object wave which gets overlayed with the second portion acting as reference field. The latter is created from the second portion of the light field by zero order spatial filtering the light field in the aperture plane at its focus on a point mirror. This spatial filter creates or revokes a plane wave after re-collimation which in turn serves as ideal reference wave for the object wave in the interferometer portion. The interferometer is a common path interferometer. They are very stable and robust to external influences from air flow or mechanical vibrations, since the sensitive interferometric portion can be built very compact.

Therefore, it is well protected to external impacts. Common path means that the entire light flux penetrates through the object and gets split up into an object wave and a reference wave after the object. Then, the object and reference waves are processed separately at some portion of the beam path before they get overlayed in the interferometer portion. The separate beam paths have to have the same optical path length to satisfy the temporal coherence condition thus leading to maximum interference contrast. In addition, a controllable shear gets applied to create an equidistant interference pattern in case of an undisturbed plane object and reference wave. Any spatial phase retardation of the object transfers into a change of the ideal (regular) interference pattern. For the evaluation of the complex images with the interference structures, the image gets Fourier transformed. Due to the shear, there appear three peaks in the Fourier pattern as shown in figure 19 for a real image. It contains a central spot as usual and two strong symmetric spots representing the first orders of the shear direction. The distance of the first order peaks from the center peak is a direct measure for the shear fringe spacing. These two side maxima are point symmetric due to the nature of the Fourier transform of two half fields of complex conjugate amplitudes.

One of these two symmetrical spots is cropped with its surrounding area. The cropping window in the shear direction has a maximum length equal to the distance from the center spot to the first order spot and is centered at the peak position of the first order spot. In the orthogonal direction, the cropping window can span the full size of the Fourier plane. The cropped area is centered (shifted) in its coordinates in the shear direction on the position of the central peak of zero order. Then, an inverse Fourier transform gets applied to reconstruct the object function. Due to the shift, the interference fringes from the shear are eliminated and the object height profile gets visible in the intensity pattern as a modulation of the intensity. In case of larger object topographies, a phase unwrapping in the image needs to be applied in order to remove artifacts in the intensity image from the wrapped phase function. In effect, the phase as determined by the digital holographic microscope serves as a direct measure of the optical height of the object. The physical height of the object can be retrieved when the difference of the refractive index from the sample and its surrounding (e.g. air or fluid) medium are known. A common method to determine the refractive index of a fluid is to disperse some spherical beads of known refractive index and high-quality spherical shape as reference in the fluid. The phase pattern can be used to determine and thus calibrate the phase retardations measured. Accordingly, the physical thickness is retrieved and thus 3D information of high resolution and precision is available. Due to the shear, a single measurement is sufficient to capture all 3D information. Thus, the exposure time of a single frame sets some limit to the motion allowed for the objects under investigation. To avoid significant motion blurring effects on the results of the measurement in 3D, the exposure time for all images has to be reasonably small to stay significantly subwavelength. Figure 20 shows some typical embodiments for setups of digital holographic microscopes. Due to the interference in the digital holographic microscope (DHM) measuring principle, unambiguous depth resolution is limited to a phase retardation of half a wavelength. The larger the shear, the smaller the depth measuring range gets in z direction. Depending on the object structure, this might be too small for a precise measurement. To enlarge the unambiguous measuring range in z, the concept of synthetic wavelength [61, 62] was introduced. In the case of two wavelengths, the useful measuring range expands to the first common overtone of the two wavelengths. This can increase the useful range by one or two orders of magnitude, depending on the central wavelengths of the two measurements. E.g. for 500 nm and 550 nm or 505 nm, respectively, a factor of 10 or 100 for the measuring range in z could be gained by the synthetic wavelength concept. The bandwidths of the light sources transform into the contrast of the fringe pattern. Figure 21 shows the principle of the concept for two wavelengths.

Figure 22 shows the application of a synthetic wavelength on an optical step object of step height 3.5 μm exceeding each individual wavelength but not the synthetic wavelength. The phase shift from the optical thickness of the step is clearly visible at the edges of the step for each wavelength. For the sake of better visibility, wavelength 1 (Lam 1) is shown with offset 0.5, wavelength 2 (Lam 2) with offset 1.5 and the signal for the synthetic wavelength (Lam 1—Lam 2) with offset 3. In this signal, an increase of the signal amplitude is clearly visible when comparing the green and the yellow plot curves. This is defined by the envelop of the synthetic wavelength interference pattern modulation.

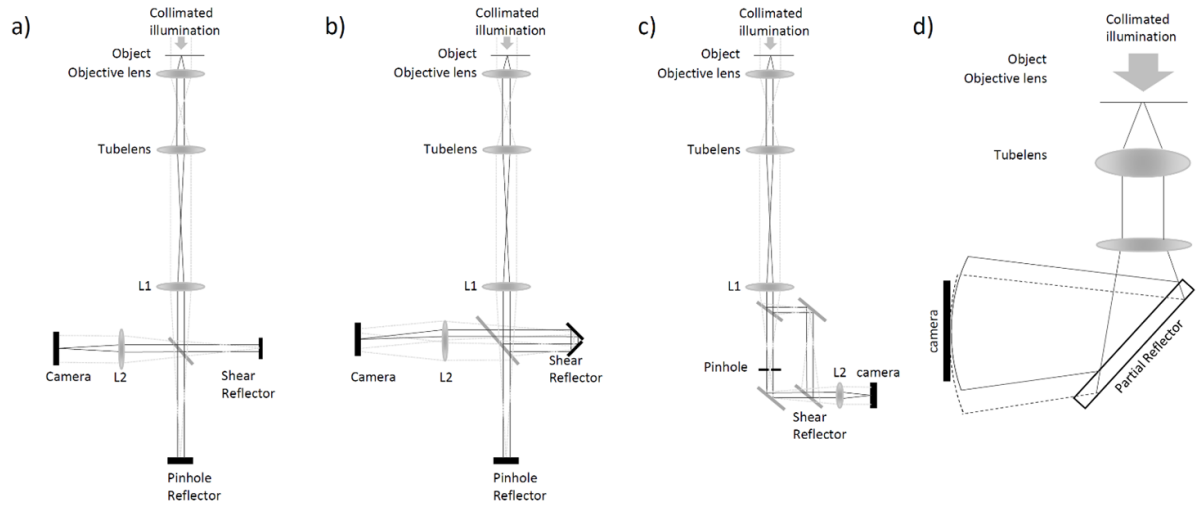

Figure 20. DHM with (a) Michelson-interferometer (b) prismatic shear reflector (c) Mach–Zehnder Interferometer and (d) partial reflector to split up the optical field to create the interference pattern.

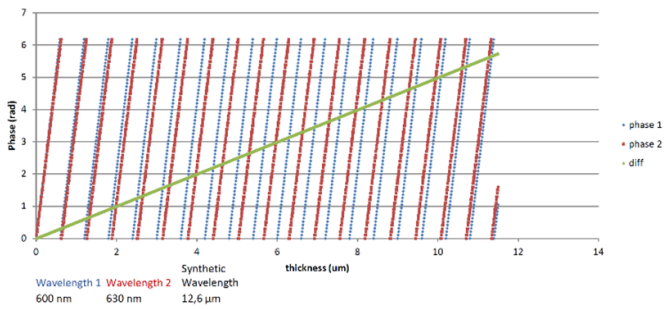

Figure 21. Concept of synthetic wavelength—schematic view for phase shift vs. depth of object for two wavelengths 600 nm and 630 nm—increase in unambiguous measuring range of factor 60.

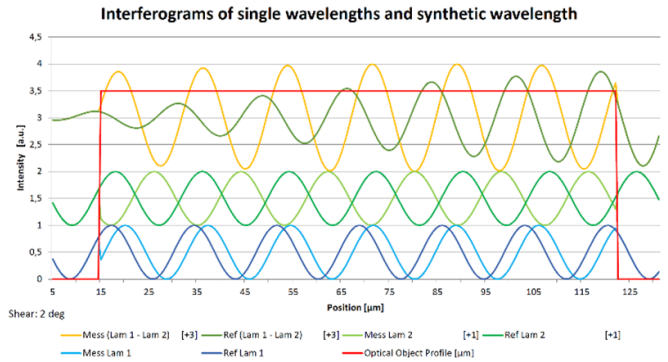

Figure 22. Simulation of the phase signal for the two wavelengths (Lam 1, Lam 2) and the difference in Phase in the summed-up signal (Lam 1—Lam 2).

5.3. Pattern projection 3D sensors

Stereoscopic triangulation sensors are very prominent and versatile systems for optical 3D measurements. The measuring principal can easily be scaled to the requirements of a given measurement task form small to large object sizes. There are two functional concepts in the field.

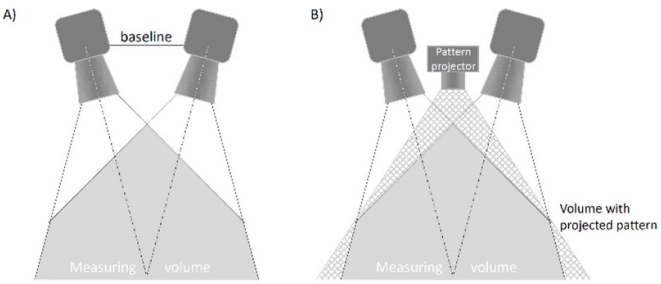

Figure 23. (A) Passive and (B) active triangulation system with two cameras shown. A minimal active triangulation system consists of only one camera plus pattern projector.

Passive triangulation uses two cameras at different positions and/or orientations to capture an image of a scene. These images are than taken to determine the 3D or depth information by evaluating the parallax effect arising from the different perspectives the object has in the two images. In this basic setup, the cameras use the light conditions of the scene as it is. That's why it is called passive. A typical setup is shown in figure 23. A. The object's topography is retrieved from the camera images by stereoscopic reconstruction of corresponding pairs of images. Ideally, images of each pair are taken synchronously to avoid any impact of object motion. The position of the two cameras and the imaging properties of each camera has to be characterized in calibration measurements. It serves to register the pixels of the two cameras with respect to each other as a function of depth as the fundamental prerequisite for depth measurement. For the calibration, a calibration artifact like a planar target with a known pattern of fiducials is positioned at various positions and/or tilted orientations inside the measuring volume of the sensor. For each position and/or orientation, a set of images is taken. The whole set of images form all the calibration measurements is then input into a global optimization algorithm to compute for the cameras relative positioning and the imaging performance of each of the cameras. In the calibration, the optical axis and thus its

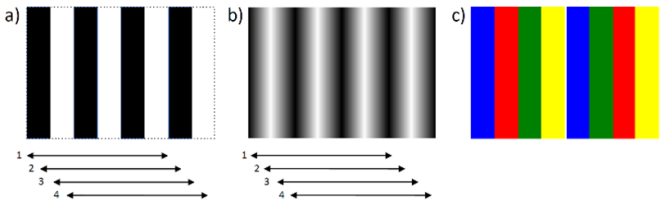

Figure 24. Typical fringe patterns for projection in active triangulation systems. (a) Binary pattern, (b) grey tone pattern and (c) colour coded pattern. The arrows below (a) and (b) show the shift of the pattern for phase shifted evaluation technology.

central axial pixel on each camera sensor are determined. The line connecting these two intersection points of the two cameras is called epipolar line [63].

The distance of these two points on this axis usually is referred to as system baseline. The length of the baseline for a given measuring distance is a key parameter for the maximal achievable depth resolution of a sensor. In principle a longer baseline corresponds to higher triangulation angles resulting in higher depth resolution. Typically, the calibration results are reported as intrinsic calibration for the camera imaging performance (like distortions etc) and extrinsic calibration for the respective spatial orientation of the cameras plus some characteristic values for the residuum as a quality index of the optimization result. For a proper scaling of the images, at least one image pair needs to contain a scale bar of known dimension or length. Corresponding features of the object in the two camera images are shifted along the direction of the epipolar line. The relative positions of these image points on the camera sensors correspond to the position and depth of the respective object feature with respect to the sensor coordinate system.

For passive triangulation systems, the object has to have unique features that can be imaged by the cameras. The lower the number of such feature points, the lower the number of 3D points gets. Objects with flat or non-textured surface without contrasting features are not compliant with this method. Objects with internal symmetries, like rotational symmetries of regular patterns can be problematic for proper reconstructions when symmetrical points get confused with the real points. To overcome this problem, active triangulation was introduced as a much more general method. Active triangulation uses an active controlled illumination system to project pre-defined light patterns in the FoV of the cameras. On the one hand, the patterns simply illuminate the scene. Typical patterns contain high contrast binary patterns of black and white lines or a sinusoidal structure or colour patterns. Exemplary patterns are shown in figure 24. On the other hand, these defined structures project artificial features also on smooth surfaces of non-textured objects. The camera captures these projected patterns all across the object in the images. The patterns may employ intensity variations, color contrast or even polarization to code structures for later evaluation [64].

Typically, a sequence of patterns is used to capture a related sequence of triangulation system images in the same arrangement of the object with respect to the sensor. Different patterns vary in the spatial frequency and/or the phase of the pattern projected. In addition, a phase shift along the epipolar line for consecutive patterns of the same period is used to get a full coverage of the object surface since the bright and dark areas are shifted typically in 3 or 4 steps across one period. In case of binary patterns—also referred to as grey tone -, only the points of the edges contribute to the number of points measured. In case of a sinusoidal pattern, the phase of each point in the FoV can be evaluated for each camera separately. This results in a dense sampling of the object's surface topography with the phase related spatial information. For fast phase evaluation, four patterns are used which are shifted by 90 degrees each. The phase map can be computed directly from the pixel intensities of the respective pixels by the formula:

$$Phase\,(Pixel) = arctan\left(\frac{\tan^{-1}(I(0)) - \tan^{-1}(I(180))}{\tan^{-1}(I(90)) - \tan^{-1}(I(270))}\right) \tag{6}$$

The images from an active stereoscopic camera get evaluated in the same way as native structures of the object to determine 3D depth information. To compute the object's surface shape, corresponding points on the object surface are identified by the projected grey tone or phase pattern for further analysis. Due to the periodicity of the pattern, the depth resolution is typically limited to one period of the pattern. The higher the spatial frequency of the pattern is, the higher the resolution but the lower the range of unambiguity. The system's depth measuring range can be increased significantly by using a sequence of different sets of patterns with different spatial frequencies from low to high values to avoid such ambiguity effects. To precisely register each pixel of the cameras, the spatial frequency of the different patterns projected preferably increases from the base frequency of one period in the image frame by a factor of two from set to set to simply combine the phase values measured. The maximum frequency is related to the resolution limit of the optical system employed. Finally, the results gained for each spatial period are merged into a 3D image of the object's topography.

In principle, it is sufficient to combine one camera with one active projector to measure 3D information. These systems are also called fringe projection systems. They capture depth information for the entire FoV of a 2-dimensional camera sensor. The calibration principle remains the same and the pixels of the camera also get precisely registered to the phase patterns of the projector. For precision metrology, it is somehow preferable to combine one projector on the symmetry axis of two cameras. Now the two cameras have a larger triangulation base and the light from the central projector does not get obstructed so much due to the smaller incidence angle. This results in a higher number of points measured. By the advent of durable powerful LEDs, there was a trend to shift the wavelength of the pattern projector into the blue in order to optimize the depth resolution of the system by the scaling factor of the shorter blue wavelength. Finally, in a real measurement, the resolution attainable is also influenced by the cooperativity of the object to the respective sensor wavelength.

In the course of time, numerous modifications of the fringe projection systems have appeared. Very different kinds of patterns were projected on the object. It ranges from single

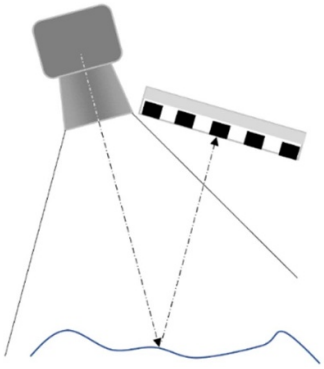

Figure 25. Schematic view of a deflectometry measurement system, where the object in the bottom is part of the beam path from the self-illuminated object to the camera.

patterns with non-periodic structures to have unique features to register the camera. Fringe projection systems with projected lines of different colors and preferably a non-periodic sequence of these colors over the entire FoV are very easy to handle. Sometimes they are called color-coded fringe projection systems.

Due to the advent of computer-generated holograms (CGH), random dot projectors can be built that have a unique dot pattern for a larger area. This pattern may reproduce after some lateral distance larger than the lateral shift of the pattern over the entire depth measuring range. This long periodic repetition of the same pattern simplifies the generation of the random dot pattern significantly and reduces the number of phase steps in the CGH and thus cost of the system. Modern compact 3D sensors (Intel Real sense [65]) with moderate measurement accuracy make use of this cheap, easy and compact to build technology. Typically, all sensors using only one pattern compromise to some extent the lateral resolution capability of the optical imaging system to have clearly distinguishable spots of the random dot pattern in a small area patch or to identify a sequence of colour steps along a line element. Depending on the object's topography, the one or the other method can be more appropriate in terms of data points measured on the object.

5.4. Deflectometry

When the object under test has a reflective surface of high quality with only a low portion of light scattering, the pattern projection technology is not efficient anymore. The problem arises from the high portion of light reflected on the object. Only little or no light gets deflected into the aperture of the camera lens. The signal gets too weak for a measurement. In addition, the signal strength depends strongly on the relative arrangement of the sensor with respect to the local surface shape and surface normal of the object. A typical setup to illustrate the principle is sketched in figure 25.

Deflectometry can be considered as a modification of triangulation measurement systems. When the surface under test has some optical quality, it can be integrated directly into the metrological beam path between the pattern generator and the camera. The projector is replaced by a display to generate test structures, or the projector projects the test structures on a diffusive surface acting as the effective location of the test structure. Now the camera images the pattern of given dimension via the surface of the part to be inspected. Thus, the surface geometry directly influences the optical beam path and as such also the shape of the patterns as seen by the camera. The basic principle to employ different patterns, preferably with sinusoidal shape of different pitches including phase shifting, like it is shown in figure 24, is used in deflectometry for inspecting high quality surfaces. The evaluation of a series of images remains the same as in active triangulation. Typically, the main interest is to find local surface damages represented by areas of pattern anomalies in the imaged patterns instead of complete 3D geometries. Defects can be found on single image level without tedious reconstruction efforts of a 3D geometry, which is much harder to measure in deflectometry, since each inspected object would require some basic calibration efforts. Mechanical fixtures for the object can be used to reduce this effort significantly.

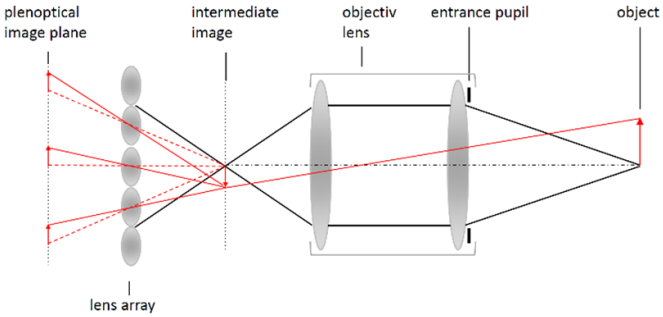

Figure 26. Schematic view of a light field camera with a micro-lens array between the objective lens and the image sensor plane.

5.5. Plenoptical camera—light field imaging

The plenoptical camera or light field camera [66–68] is a multi-aperture camera. The functional principle was described in 1902 already [69]. Since camera sensors and computing hardware were not available for a long time, it took about 60–100 years that this concept made some significant progress in research and gained some economic relevance. Typical setups have one main imaging lens plus a micro-lens array in a given distance to the sensor array as sketched in figure 26. The micro-lenses are arranged in a rectangular grid or a honeycomb array in order to maximize the utilization of camera chip pixels by minimizing the area between neighboring sub-images from the discrete lenses of the micro-lens array. The NA of the main lens has to be matched with the micro-lens NA to fill the camera sensor optimally with an array of sub-aperture images. The lens centers of the micro-lenses serve as basis for the local triangulation of corresponding features of neighboring sub-images for the depth estimation of this respective image feature. In a calibration step, the respective lens center position of every micro-lens is determined. The

lens center is important for a ray tracing-based reconstruction of the depth information for a given feature point. For every corresponding point in different sub images the central rays are traced back from the image point through the center of the respective lens to their point of intersection in the measurement volume. Due to small errors for the true feature position on the sensor, the intersection is usually more like a small region of closest distance for all the rays traced back in the object space. Dependent on the distance between object and lens, the number of sub-images available for multi-triangulation for a feature varies from a minimum of two up to a typical maximum of seven. Perwass and Perwass [70] introduced a honeycomb type of micro-lens array with a cluster of three types of micro-lenses of different focal length as a unit cell of the micro-lens array in order to increase the measuring range of the plenoptical camera significantly [70–72]. In general, some portion of the maximal achievable lateral resolution of the camera sensor gets sacrificed in this sensing principle with the reduced image magnification by the micro-lenses in order to achieve a depth measurement in a single camera frame. The plenoptical camera principle is capable of taking 3D images of a scene at video rates and even much faster by pushing the demand on the computing power for image analysis in frame rate speed. Typically, the combination of main lens and micro-lens reduces the lateral resolution by a factor of 2–3 compared to imaging with a standard camera with the same lens.

On the other hand, the DoF can be increased by about the same factor with the micro-lens array with different lens types, so that the effective DoF and thus the measuring volume is increasing significantly. This feature is of particular interest for imaging systems like microscopes with a high NA at the object and thus a very shallow DoF, often not capable to capture the entire thickness of a sample like a single cell of a biological sample. The reconstruction techniques for plenoptical images allow to display different representations of the light field captured, like a total focus image or the image as if it would have been captured with the unchanged main lens with significantly lower DoF or a depth map of the entire FoV.

Alternatively, in micro-optically integrated setups a micro-lens array is used directly as imaging lens. It is attached to the camera sensor, so that this setup can be considered as an array of multiple cameras separated by the pitch of the lenses in the array. This mimics the structure of the eye some insects do have like dragon flies. To avoid crosstalk between neighboring channels in the micro-lens array, some light shield or baffle layer is attached to the lens array [73]. In addition, this setup was combined with a narrow band dichroic linear variable filter (LVF) to make this camera colour sensitive in the individual sub-cameras for multi- or hyperspectral imaging applications. To optimize the setup, the direction of the chirp axis of the LVF is rotated with respect to the axis of the rectangular grid of the micro-lens array, so that the visible spectrum was covered with e.g. 64 colour channels with a shift in central bandwidth of about 6 nm. This very compact camera is capable of measuring 3D information with up to 64 corresponding feature points of the sub-images supplemented by spatially resolved spectral information in 64 separated colour channels.

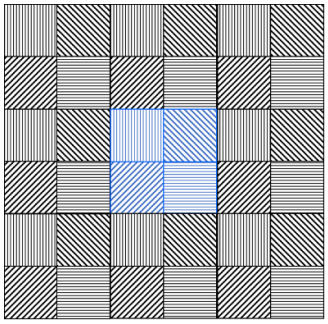

Figure 27. Schematic diagram for a chip area of a polarization sensitive camera with polarization filters under 0, 45, 90 and 135 degrees.

This compact camera type can be described as 3D multispectral camera.

6. Conclusive aspects, trends and outlook

This article is intended to provide the reader with a wide selection of technologies and sensor types for 3D metrology. This may help the intrigued reader even to grasp the key functional principle of sensors not covered in this selection as this can never be fully exhaustive. Links to textbooks may help to find additional information like technical details or formulas.

Furthermore, for some of the sensors the chain of innovation and evolutionary steps is shown exemplary to give at least some hints how functional needs and technical feasibility can cross-fertilize over time. This may help to get a first impression of how new technical capabilities can be utilized to improve the sensor and its metrological performance over time. Examples are: more advanced and robust spectral sensing capabilities by FBG [22, 74] based ultra-compact and cost effective spectrometers, 2D spectral sensing with LVF [75] or tunable dichroic filters [76] for scanning wavelength ranges over time. This may be paired with new sensors of improved quantum efficiency leading to higher sensitivity, to new photosensitive materials of mixed and/or layered material to cover the huge spectral range from 400–2000 nm, i.e. entire visible and short-wave infrared range, with a single point or camera sensor.

New sensor structures or functional modalities can be another source for innovation. A polarization camera enables to measure the light's polarization state paired with spatial resolution in an area of 2×2 pixels with four polarizers at 0, 45, 90 and 135 degrees as shown in figure 27.

From this raw sensor signals the polarization state, degree of polarization, polarization angle and portion of unpolarized light can be retrieved from the data measured to create four views of the same scene from a single image capture. The polarization angle determination is mathematically the same as for the evaluation of phase shifted active pattern projection from equation (6).

The formula reads now:

$$2\,\alpha_{i,j} = \arctan\left(\frac{I_{i+1,j+1}(90) - I_{i,j}(0)}{I_{i+1,j+1}(135) - I_{i,j+1}(45)}\right). \qquad (7)$$

Please note, that a small trick with a factor 2 gets applied to use the double angle 2α and that the angular values for the polarization filters on the camera are doubled, too, where *i, j* are the indices of the respective pixel.

To compute the polarization state, degree of polarization and portion of unpolarized light the following definitions and formulas get applied:

$$I_{\mathrm{Unpol}\,i,\,j} = I_{i,j}(0) + I_{i,j}(45) + I_{i,j}(90) + I_{i,j}(135) \tag{8}$$

$$I_{\mathrm{Pol}\,i,\,j} = \sqrt{\left(I_{i,j}(0) - I_{i,j}(90)\right)^2 + \left(I_{i,j}(45) + I_{i,j}(135)\right)^2} \tag{9}$$

where $I_{i,j}$ are the local intensity of pixel $I_{i,j}$ or the interpolated pixel intensities of the respective polarization type from the nearest neighbor pixels.

The degree of polarization is defined as

$$DoP_{i,\,j} = I_{\mathrm{Pol}\,i,\,j}\left(0{,}5 \times I_{\mathrm{Pol}\,i,\,j} + I_{\mathrm{Unpol}\,i,\,j}\right). \tag{10}$$

The advent of polarization cameras might help to integrate different imaging modalities into one of the sensor types described before to enable new or more robust measuring modalities. For example, a polarization camera might enable to securely detect multiple reflections or stray light on an object in a laser triangulation probe and make the entire system much more robust and in turn increases the usability.

Another innovative product is the event camera [77] or dynamic vision sensor. They do not read a full camera frame at a pre-defined given frame rate or exposure time like in global or rolling shutter cameras. Event cameras typically have a configurable threshold for the sensor where a pixel only fires an event when the value of the pixel changes by a threshold increment in positive or negative direction. This procedure mimics the base function of the human eye and allows to have self-adopting and different activities for every pixel in the sensor based on the image content. The sensor signal is a time sequence of stochastic nature. One information unit consists of pixel coordinate in x and y, exact time and polarity of change direction of the pixel value in form of ± 1 increment of the threshold value. In consequence, data bandwidth is spent for more active pixels and data from non-active pixels gets reduced or even suppressed which also implies some novelty filtering and making the transmitted data 'more relevant' — at least for dynamic scenarios. In consequence, a classical 2D image needs to be composed in a computing device outside the camera. Thus, much higher effective frame rates, shorter exposure times and thus also dynamic ranges can be realized compared to standard camera operating modes. There are already camera designs combining classical image capture and event camera operation in a single system [77]. These cameras are called DAVIS cameras. Since the data stream of event cameras is completely different compared to the frame-based data structure of more classical cameras, performant image processing algorithms have to be adopted to the new kind of data stream in order to exploit the full potential of this sensing approach. In principle, the cameras mentioned in the descriptions in this paper can mostly be replaced by event cameras. By doing so, the modified sensor will exhibit new features and capabilities. Time will show how new sensor structures and modalities will enable considerable technical evolution and innovation of sensors. The trend to much higher pixel numbers in sensor arrays in the range of some 10 Mpxl (Megapixel) at reasonable cost and still low dark noise will enable new sweet spots where to tweak a given sensor principal for new performance levels and applications.

Light sources are another major source for innovation in sensors, since higher quantum efficiency, smaller size and increased brilliance, new wavelengths, controllable (effective) or narrower bandwidth or shorter switching times are some of the main routes in R&D and for the markets.

Furthermore, increasing local computing power allows for more elaborate sensor data evaluation schemes. New generative imaging modalities like the Fourier ptychography allow to synthesize high resolution, high DoF and large FoV images from a larger number of low-resolution sub images with large FoV. New sensor types will enable further new concepts for even more advanced image fusion scenarios even for different modalities.

More computing power from central processing unit (CPU) [78], graphics processing unit (GPU) [79] or field programmable gate array (FPGA) [80] and the like allow to integrate high fidelity data operations to apply machine learning [81] or artificial intelligence (AI) [82] or bionic image processing algorithms [83] on or for the sensor. These functions may be pre-trained and loaded into the sensor or even trained directly on the sensor. This might help to optimize sensor signal data. On the other side, care has to be taken to not sacrifice data or image content by any adversarial side effects from data pre- and postprocessing. Data quality of the sensor needs to be qualified thoroughly for metrological applications. It is the key to the future success of metrology in general. Figure 28 shows a schematic from the GEMIMEG-II [84] project, where DCC [1] are developed to fully digitize the quality infrastructure.

The goal of the project is to exchange the data seamlessly between different systems without a media break and to make calibration data machine readable, machine interpretable and machine executable. DCCs can also convey much more details and calibration related information compared to its predecessor on paper or static pdf documents. This additional data in turn can be used in later applications of the sensor or a sensor system, since these data are available in machine readable, machine interpretable and machine actionable formats. Figure 29 shows a generic view on the content blocks of a DCC and the related process with a digital calibration request (DCR) to initiate technically a specific calibration. A digital calibration answer (DCA) might convey all the information not contained in the DCC but requested by the issuer of the DCR.

The diagram of figure 30 shows a quality indicator QoX, where measurement values are characterized by QoS, processed data by QoD and derived information by quality of information (QoI).

This concept is still under development, so that a measured datum may consist of the measurement value as measured and corrected for deterministic errors plus the metrological

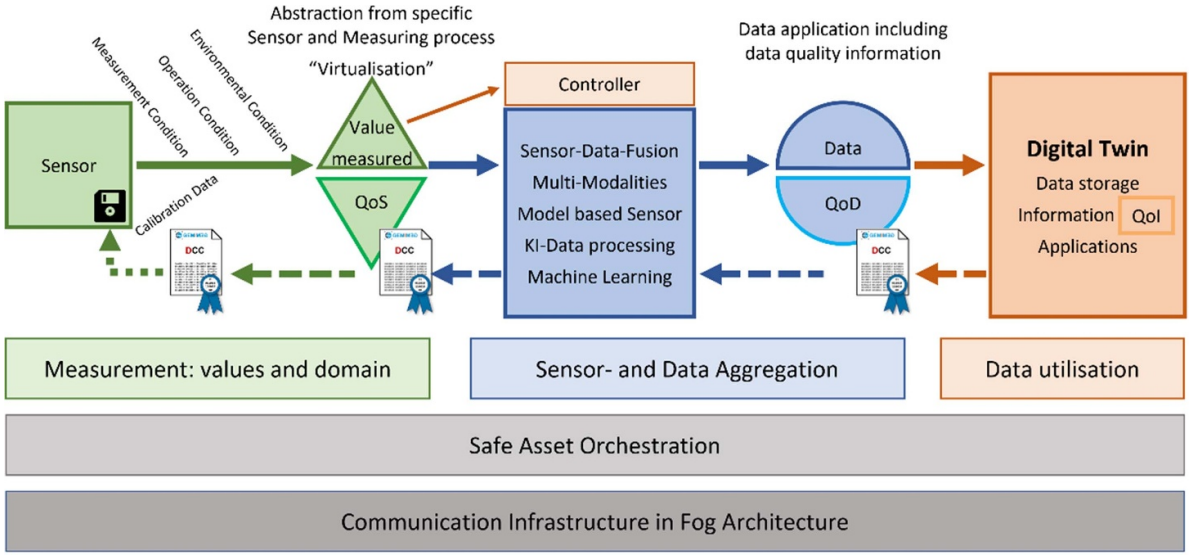

Figure 28. Schematic diagram for data processing in quality infrastructure—including full backward traceability of the DCC or QoX from data/ information back to the sensor as shown in the GEMIMEG-II structural view chart.

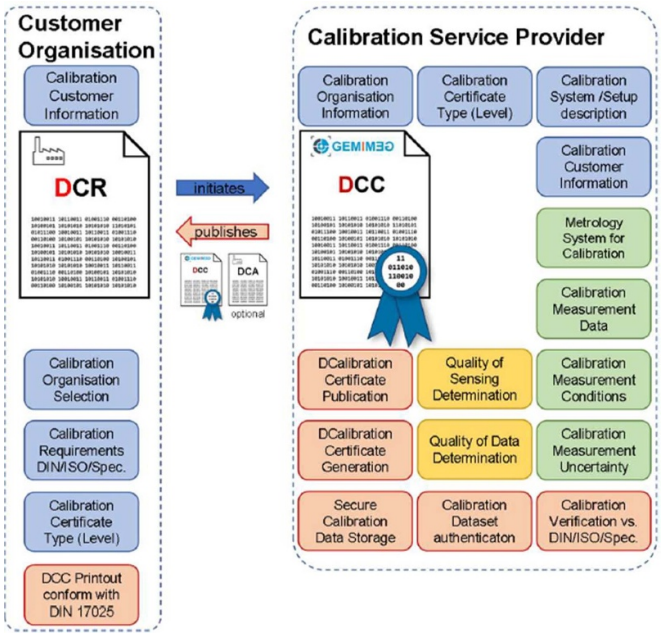

Figure 29. Schematic diagram of the DCC process and its relation to DCR and DCA.

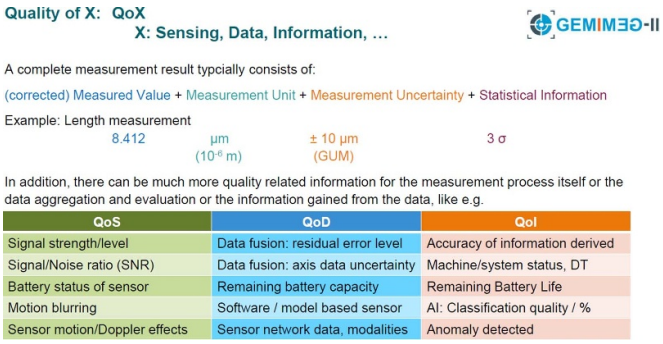

Figure 30. The Quality of X (X: Sensing, Data, Information) concept with some examples. Colour code of domains according to figure 28.

uncertainty according to the guide to the expression of uncertainty in measurement (GUM) [85] plus the QoS information as a simple indicator of a 'trust level' to be associated with the datum value. The QoX values can be used in the data processing domain by data experts to e.g. assign weights to the datum when using it to generate new data or information. This quality information is assigned to the datum at a stage, where still domain specific know how for the respective step of processing is available. This know-how may comprise of e.g. the respective measurement conditions or details of the data processing steps and/or information generation process, respectively. The detailed description of sensor principles may help to derive valuable QoS quality indicators for a given measurement system. A very simple example for a quality of sensing indicator could be the SNR as it is defined in the range from 0 to 1. Preferably, QoX values should be in the Range [0, 1] to simplify further steps of data aggregation or fusion.

When the values of one or multiple sensors get processed to data, also the related single or multiple QoS should be processed into new (single) QoD value(s) to characterize the quality level of the output data. For processing the QoX, for example the arithmetic or geometric mean can be used. For more complicated use cases, the QoX of individual data sources can be weighted and the weights can be processed in the way known for weighted arithmetic or weighted geometric mean values [86]. This concept will help to transfer the valuable gut feeling of a metrologist into the chain of digital metrology and to pave the way into fully automated data utilization and analysis scenarios. By this approach, some information on boundary conditions or 'observations' around the measurement which are not affecting the results directly

can be captured and conveyed to later steps of data utilization or information generation. The QoX can serve to generate information on the trust level associated with the data created. The same concept gets applied when information is derived from data. A QoI value related to the information is generated to characterize the trust level of the respective information. This concept may be of great value even in 3D metrology, when measured data of different sensors and/or modalities get merged or fused into one final result of higher accuracy and/or trust level [87]. In future perspective for model based or even AI based sensors, the QoX might become of key importance when assessing the quality or trust level of the results gained from these sensors.

In contrast to physical sensors, model-based sensors or AI based sensors are software based and rely on the applicability of the model or the coverage of the parameter space by the training data set. When applying such a software-based sensor which is fed by measuring data of one or multiple other physical sensors or even software-based sensors, it is important that the input data stem from a data range also used for deriving or training the software-based sensor. This is called out of distribution detection [88, 89] or in some cases also input space verification when looking on the parameter space used for the training. Software based sensors might show a very strong nonlinear behavior outside the parameter space used in the definition and training phase. In consequence, the output of such sensors might be highly susceptible even to small parameter changes of the input parameters when they are out of the parameter space used when training the sensor. A QoD or QoI could describe, if the sensor operation is covered in the training by e.g. a Boolean variable or how stable the result is in some relative metrics when the input values are changing slightly. This field is quite new and subject in different research activities of present and upcoming metrological projects. To solve this question is one of the important issues when a software-based sensor has to be calibrated and calibration results have to be documented in a (digital) calibration certificate. Typically, calibration certificates list the operational conditions of a sensor, when the calibration is applicable. This has to be transferred into the digital world of digital metrology and truly digital industries in a robust and machine readable and machine interpretable way. Just for illustration purposes, figure 30 shows some more examples of the QoX concept in practical applications.

Even the field of resolution in a measurement is still under thorough discussion and consideration [90]. All factors influencing the result of a measurement directly or indirectly have still to be treated according to the guidance of the GUM [85], the guide to the uncertainty of measurement.

For machine readability and machine interpretability of the QoX, a precisely defined semantics needs to be developed. A first structural concept is shown in figure 31. This description needs to be clearly defined in its functional elements in order to be open in its application even for QoX values and types not foreseen in the definition phase of the generic concept. In this respect, also the name of a QoX and the respective definition, its computation formula and related scale are of fundamental importance. QoX can even be used and of great value

Sensor System Type	Type of physical sensor or software/model based sensor
Quality Indicator	Sensor System parameter to be characterized internal parameter: e.g. operational, functional external parameter: e.g. environmental
Indicator Description Definition	Detailed/explicit determination scheme, traceable, version controlled formula for calculation incl. input parameters allowed range of values, value type
Indicator Metric	Scale for Indicator (absolute + unit, relative, %, dB, …)
Indicator interpretation:	Status interpretation (good, acceptable, bad, info only – low trust level, …)
…	

Figure 31. The quality of X concept for a given sensor and a set of functional elements describing the respective QoX.

to determine if a dataset can be used for a given application, coming up much later than the data was measured. For a given applicational context or dataset, the definition of the QoX has to be unique and traceable in versions, if changes might be applied over time [91].

This concept may become of significant value in an internet of things scenario, when different smart sensors are combined on purpose for a metrological task—like to produce a stereoscopic 3D image from different cameras capturing an overlapping scene from different viewing angles even at slightly different instances of time. The concept may than be applied to the camera pose, the image capture time in a common time zone and the like, where multiple factors of influence need to be considered for metrological applications where a known level of accuracy and precision matters.

This outlook cannot be exhaustive at all but should raise at least some of the important aspects we will face technically and also initiated by the digital transformation in the field of (optical 3D) metrology in the next years.

Data availability statement

No new data were created or analysed in this study.

Acknowledgments

The author is so grateful to so many colleagues I met during my career for numerous valuable discussions about optics and metrology. Insights from these discussions helped me so much to broaden and deepen my knowledge about (optical) metrology. Since it is impossible to mention all of them here, I want to thank all of them in this general fashion. I hope the selection of topics in this topical review may be as valuable for interested readers like the discussions were for me.

The research in the GEMIMEG-II project are funded by the German ministery for economy affairs and climate action on the basis of a decision by the German Bundestag under Grant No. 01 MT20001A.

ORCID iD

Thomas Engel https://orcid.org/0000-0002-6155-2760

References

[1] DCC_PTB *Digital Calibration Certificate* (available at: www.ptb.de/dcc/) (Accessed 27 June 2022)

[2] Eichstädt S *et al* 2017 Metrologie für die Digitalisierung von Wirtschaft und Gesellschaft *PTB-Mitt. Band* **127** 2263156

[3] Hutzschenreuter D *et al* 2021 SmartCom Digital-SI (D-SI) XML exchange format for metrological data version 2.0.0 (available at: https://zenodo.org/record/4709001) (Accessed 10 March 2022)

[4] Volkmann H 1966 Ernst Abbe and his work *Appl. Opt.* **5** 1720–31

[5] Born M and Wolf E 2013 *Principles of Optics: Electromagnetic Theory of Propagation, Interference and Diffraction of Light* (Amsterdam: Elsevier)

[6] Koelsch P 2006 *Herbert Gross (Ed.): Handbook of Optical Systems* (Berlin: Springer)

[7] Török P and Kao F-J 2007 *Optical Imaging and Microscopy: Techniques and Advanced Systems* vol 87 (Berlin: Springer)

[8] Gross H, Blechinger F and Achtner B 2008 Microscope optics *Handbook of Optical Systems: Volume 4: Survey of Optical Instruments* vol 4 pp 541–721

[9] Wikipedia Sinc function 08 2022 (available at: https://en.wikipedia.org/w/index.php?title=Sinc_function&oldid=1109119107) (Accessed 26 September 2022)

[10] Stenger F 1981 Numerical methods based on Whittaker cardinal, or sinc functions *SIAM Rev.* **23** 165–224

[11] Rayleigh L 1879 XXXI. Investigations in optics, with special reference to the spectroscope *London, Edinburgh Dublin Phil. Mag. J. Sci.* **8** 261–74

[12] Sparrow C M 1916 On spectroscopic resolving power *Astrophys. J.* **44** 76

[13] Gensun F 1996 Whittaker–Kotelnikov–Shannon sampling theorem and aliasing error *J. Approx. Theory* **85** 115–31

[14] Wikipedia STED microscopy 2022 (available at: https://en.wikipedia.org/w/index.php?title=STED_microscopy&oldid=1092469074) (Accessed 26 September 2022)

[15] Hell S W and Wichmann J 1994 Breaking the diffraction resolution limit by stimulated emission: stimulated-emission-depletion fluorescence microscopy *Opt. Lett.* **19** 780–2

[16] Wikipedia Signal-to-noise ratio 2022 (available at: https://en.wikipedia.org/w/index.php?title=Signal-to-noise_ratio&oldid=1104835005) (Accessed 26 September 2022)

[17] Wikipedia Depth of field 2022 (available at: https://en.wikipedia.org/w/index.php?title=Depth_of_field&oldid=1109010812) (Accessed 26 September 2022)

[18] Wikipedia Charge-coupled device 2022 (available at: https://en.wikipedia.org/w/index.php?title=Charge-coupled_device&oldid=1111316375) (Accessed 26 September 2022)

[19] Wikipedia 2022 CMOS 18 September (available at: https://en.wikipedia.org/w/index.php?title=CMOS&oldid=1110955832) (Accessed 26 September 2022)

[20] Technology Sony semiconductor solutions group (available at: www.sony-semicon.com/en/technology/index.html) (Accessed 26 September 2022)

[21] AR84042A1 (available at: http://depatisnet.dpma.de/DepatisNet/depatisnet?action=bibdat&docid=AR000000084042A1) (Accessed 26 September 2022)

[22] Thiel M, Flachenecker G and Schade W 2012 Direct writing of Bragg grating structures in waveguide bundles *Advanced Photonics Congress* pp JM5A–57 Optica Publishing Group

[23] Meyer J, Nedjalkov A, Kelb C, Strobel G J, Ganzer L and Schade W 2020 Manufacturing and characterization of femtosecond laser-inscribed Bragg grating in polymer waveguide operation in an IR-A wavelength range *Sensors* **20** 249

[24] Egger M D and Petráň M 1967 New reflected-light microscope for viewing unstained brain and ganglion cells *Science* **157** 305–7

[25] NIPKOW Paul DE30105A (available at: http://depatisnet.dpma.de/DepatisNet/depatisnet?action=bibdat&docid=DE000000030105A) (Accessed 26 September 2022)

[26] Kooijman C S DE69109230T2 (available at: http://depatisnet.dpma.de/DepatisNet/depatisnet?action=bibdat&docid=DE000069109230T2) (Accessed 26 September 2022)

[27] *Wikipedia* 2020 Position sensitive device 21 September (available at: https://en.wikipedia.org/w/index.php?title=Position_sensitive_device&oldid=979631164) (Accessed 26 September 2022)

[28] Hamamatsu Photonics *Position-sensitive detectors (PSDs)* (available at: www.hamamatsu.com/eu/en/product/optical-sensors/distance-position-sensor/psd.html) (Accessed 26 September 2022)

[29] Yang M 2021 Optical distance measuring method and optical distance measuring device US10908290B2 2 February (available at: https://patents.google.com/patent/US10908290B2/en) (Accessed 12 September 2022)

[30] Hobby J, Kovacich R and Weidmann D CA3147485A1 (available at: http://depatisnet.dpma.de/DepatisNet/depatisnet?action=bibdat&docid=CA000003147485A1) (Accessed 26 September 2022)

[31] Halliday D, Resnick R and Walker J 2013 *Fundamentals of Physics* (New York: Wiley)

[32] Schwenke H, Knapp W, Haitjema H, Weckenmann A, Schmitt R and Delbressine F 2008 Geometric error measurement and compensation of machines—an update *CIRP Ann.* **57** 660–75

[33] Ambrósio R J, Valbon B F, Faria-Correia F, Ramos I and Luz A 2013 Scheimpflug imaging for laser refractive surgery *Curr. Opin. Ophthalmol.* **24** 310–20

[34] Tolt G, Grönwall C and Henriksson M 2018 Peak detection approaches for time-correlated single-photon counting three-dimensional lidar systems *Opt. Eng.* **57** 031306

[35] Fisher R B and Naidu D K 1996 A comparison of algorithms for subpixel peak detection *Image Technology: Advances in Image Processing, Multimedia and Machine Vision* ed J L C Sanz (Berlin: Springer) pp 385–404

[36] Beuth Verlag GmbH DIN EN ISO 10360-7: 2011-09, Geometrische Produktspezifikation (GPS)_- Annahme- und Bestätigungsprüfung für Koordinatenmessgeräte (KMG)_- Teil_7: KMG mit Bildverarbeitungssystemen (ISO_10360-7:2011); Deutsche Fassung EN_ISO_10360-7:2011 (available at: www.beuth.de/de/-/-/135212430) (Accessed 13 September 2022)

[37] Engel T and Winterot J EP2883018B1 (available at: http://depatisnet.dpma.de/DepatisNet/depatisnet?action=bibdat&docid=EP000002883018B1) (Accessed 13 September 2022)

[38] Engel T EP2847542B1 (available at: http://depatisnet.dpma.de/DepatisNet/depatisnet?action=bibdat&docid=EP000002847542B1) (Accessed 13 September 2022)

[39] Berner A, Degen A, Engel T and Haverkamp N DE102013112186A1 (available at: http://depatisnet.dpma.de/DepatisNet/depatisnet?action=bibdat&docid=DE102013112186A1) (Accessed 13 September 2022)

[40] Engel T and Herbig V DE10112947A1 (available at: http://depatisnet.dpma.de/DepatisNet/depatisnet?action=bibdat&docid=DE000010112947A1) (Accessed 13 September 2022)

[41] Dorn E 1900 *Zeitschrift für Instrumentenkunde* (Springer) (available at: http://archive.org/details/zeitschriftfrin06gergoog) (Accessed 13 September 2022)

[42] Platt B C and Shack R 2001 History and principles of Shack-Hartmann wavefront sensing *J. Refract. Surg.* **17** S573–7

[43] Dörband B, Müller H and Gross H 2012 *Handbook of Optical Systems, Volume 5: Metrology of Optical Components and Systems* (New York: Wiley)

[44] Levenberg K 1944 A method for the solution of certain non-linear problems in least squares *Q. Appl. Math.* **2** 164–8

[45] Marquardt D W 1963 An algorithm for least-squares estimation of nonlinear parameters *J. Soc. Ind. Appl. Appl. Math.* **11** 431–41

[46] Gerchberg R W 1972 A practical algorithm for the determination of plane from image and diffraction pictures *Optik* **35** 237–46

[47] Engel T and Gross H EP1631809B1 (available at: http://depatisnet.dpma.de/DepatisNet/depatisnet?action=bibdat&docid=EP000001631809B1) (Accessed 13 September 2022)

[48] Weisstein E W *Zernike Polynomial* (available at: https://mathworld.wolfram.com/) (Accessed 13 September 2022)

[49] Engel T and Gross H 2010 Method for determining the image quality of an optical imaging system US7831105B2 9 November (available at: https://patents.google.com/patent/US7831105B2/en) (Accessed 12 September 2022)

[50] Buttgereit U and Perlitz S 2009 Investigation of phase distribution using Phame in-die phase measurements *Proc. SPIE* **7272** 727217

[51] Buttgereit U, Birkner R, Seidel D, Perlitz S, Philipsen V and De Bisschop P 2009 Phase behavior through pitch and duty cycle and its impact on process window *Proc. SPIE* **7379** 737916

[52] Phillips Z F *et al* 2015 Multi-contrast imaging and digital refocusing on a mobile microscope with a domed LED array *PLoS One* **10** e0124938

[53] Wikipedia 2022 Ptychography 30 June (available at: https://en.wikipedia.org/w/index.php?title=Ptychography&oldid=1095727523) (Accessed 26 September 2022)

[54] Edmund Optics USAF targets (available at: www.edmundoptics.com/c/usaf-targets/1390/) (Accessed 26 September 2022)

[55] Ou X, Horstmeyer R, Zheng G and Yang C 2015 High numerical aperture Fourier ptychography: principle, implementation and characterization *Opt. Express* **23** 3472–91

[56] Kim M K 2010 Principles and techniques of digital holographic microscopy *Proc. SPIE* **1** 018005

[57] Tahara T, Otani R, Omae K, Gotohda T, Arai Y and Takaki Y 2017 Multiwavelength digital holography with wavelength-multiplexed holograms and arbitrary symmetric phase shifts *Opt. Express* **25** 11157–72

[58] Naydenova I 2011 *Advanced Holography: Metrology and Imaging* (Rijeka: BoD—Books on Demand)

[59] Interphako Home (available at: www.interphako.at/). (Accessed 13 September 2022)

[60] Girshovitz P and Shaked N T WO2013140396A1 (available at: http://depatisnet.dpma.de/DepatisNet/depatisnet?action=bibdat&docid=WO002013140396A1) (Accessed 13 September 2022)

[61] Willomitzer F, Rangarajan P V, Li F, Balaji M M, Christensen M P and Cossairt O 2021 Fast non-line-of-sight imaging with high-resolution and wide field of view using synthetic wavelength holography *Nat. Commun.* **12** 1–11

[62] Willomitzer F, Rangarajan P V, Li F, Balaji M M, Christensen M P and Cossairt O 2019 Synthetic wavelength holography: an extension of Gabor's holographic principle to imaging with scattered wavefronts arXiv:1912.11438

[63] Wikipedia 2022 Epipolar geometry 19 January (available at: https://en.wikipedia.org/w/index.php?title=Epipolar_geometry&oldid=1066620664) (Accessed 26 September 2022)

[64] Huang X, Bai J, Wang K, Liu Q, Luo Y, Yang K and Zhang X 2017 Target enhanced 3D reconstruction based on polarization-coded structured light *Opt. Express* **25** 1173–84

[65] Intel® RealSense™ Technology *Intel* (available at: www.intel.com/content/www/us/en/architecture-and-technology/realsense-overview.html) (Accessed 26 September 2022)

[66] Ives H E 1928 A camera for making parallax panoramagrams *J. Opt. Soc. Am.* **17** 435–9

[67] Adelson E H and Wang J Y 1992 Single lens stereo with a plenoptic camera *IEEE Trans. Pattern Anal. Mach. Intell.* **14** 99–106

[68] Ng R, Levoy M, Brédif M, Duval G, Horowitz M and Hanrahan P 2005 Light field photography with a hand-held plenoptic camera *PhD Thesis* Stanford University

[69] Ives F E US725567A (available at: http://depatisnet.dpma.de/DepatisNet/depatisnet?action=bibdat&docid=US000000725567A) (Accessed 13 September 2022)

[70] Perwass U and Perwass C 2013 Digital imaging system, plenoptic optical device and image data processing method US8619177B2 31 December (available at: https://patents.google.com/patent/US8619177B2/pt-PT) (Accessed 13 September 2022)

[71] Perwass C and Wietzke L 2012 Single lens 3D-camera with extended depth-of-field *Human Vision and Electronic Imaging XVII* vol 8291 pp 45–59

[72] Heinze C, Spyropoulos S, Hussmann S and Perwaß C 2016 Automated robust metric calibration algorithm for multifocus plenoptic cameras *IEEE Trans. Instrum. Meas.* **65** 1197–205

[73] emberion.com *Emberion* (available at: www.emberion.com/products/) (Accessed 13 September 2022)

[74] Wikipedia 2022 Fiber Bragg grating 2 August (available at: https://en.wikipedia.org/w/index.php?title=Fiber_Bragg_grating&oldid=1101977707) (Accessed 26 September 2022)

[75] Wikipedia 2022 Optical filter 26 July (available at: https://en.wikipedia.org/w/index.php?title=Optical_filter&oldid=1100601800) (Accessed 26 September 2022)

[76] Wikipedia 2022 Fabry–Pérot interferometer 13 September (available at: https://en.wikipedia.org/w/index.php?title=Fabry%E2%80%93P%C3%A9rot_interferometer&oldid=1110064836) (Accessed 26 September 2022)

[77] Gallego G *et al* 2020 Event-based vision: a survey *IEEE Trans. Pattern Anal. Mach. Intell.* **44** 154–80

[78] Wikipedia 2022 Central processing unit 20 September (available at: https://en.wikipedia.org/w/index.php?title=Central_processing_unit&oldid=1111329908) (Accessed 26 September 2022)

[79] Wikipedia 2022 Graphics processing unit 20 September (available at: https://en.wikipedia.org/w/index.php?title=Graphics_processing_unit&oldid=1111307459) (Accessed 26 September 2022)

[80] Wikipedia 2022 Field-programmable gate array 13 September (available at: https://en.wikipedia.org/w/index.php?title=Field-programmable_gate_array&oldid=1110109529) (Accessed 26 September 2022)

[81] Wikipedia 2022 Machine learning 26 September (available at: https://en.wikipedia.org/w/index.php?title=Machine_learning&oldid=1112463372) (Accessed 26 September 2022)

[82] Wikipedia 2022 Artificial intelligence 21 September (available at: https://en.wikipedia.org/w/index.php?title=Artificial_intelligence&oldid=1111591724) (Accessed 26 September 2022)

[83] Berco D and Shenp Ang D 2019 Recent progress in synaptic devices paving the way toward an artificial cogni-retina for bionic and machine vision *Adv. Intell. Syst.* **1** 1900003

[84] Gemimeg-Team 2022 *Gemimeg Startseite* 29 June (available at: www.gemimeg.ptb.de/gemimeg-startseite/) (Accessed 19 July 2022)
[85] BIPM *Guide to the Expression of Uncertainty in Measurement (GUM)* (available at: www.bipm.org/en/publications/guides/gum.html) (Accessed 7 February 2022)
[86] Bronshtein I N, Semendyayev K A, Musiol G and Mühlig H 2015 *Handbook of Mathematics* (Berlin: Springer) (available at: https://books.google.de/books?id=5L6BBwAAQBAJ)
[87] Engel T EP3077763B1 (available at: depatisnet.dpma.de/DepatisNet/depatisnet?action=bibdat&docid=EP000003077763B1) (Accessed 13 September 2022)
[88] Scholl C, Tobola A, Ludwig K, Zanca D and Eskofier B M 2021 A smart capacitive sensor skin with embedded data quality indication for enhanced safety in human–robot interaction *Sensors* **21** 7210
[89] Zhang Y, Meratnia N and Havinga P J 2013 Distributed online outlier detection in wireless sensor networks using ellipsoidal support vector machine *Ad Hoc Netw.* **11** 1062–74
[90] Horstmeyer R, Heintzmann R, Popescu G, Waller L and Yang C 2016 Standardizing the resolution claims for coherent microscopy *Nat. Photon.* **10** 68–71
[91] Vedurmudi A P, Neumann J, Gruber M and Eichstädt S 2021 Semantic description of quality of data in sensor networks *Sensors* **21** 6462